Generation of arbitrarily polarized muon pairs via polarized e^-e^+ collision

Zhi-Wei Lu,[1] Qian Zhao,[1,*] Feng Wan,[1] Bo-Chao Liu,[1] Yong-Sheng Huang,[2,3] Zhong-Feng Xu,[1] and Jian-Xing Li[1,†]

[1]*Ministry of Education Key Laboratory for Nonequilibrium Synthesis and Modulation of Condensed Matter, Shaanxi Province Key Laboratory of Quantum Information and Quantum Optoelectronic Devices, School of Physics, Xi'an Jiaotong University, Xi'an 710049, China*

[2]*School of Science, Shenzhen Campus of Sun Yat-sen University, Shenzhen 518107, People's Republic of China*

[3]*Institute of High Energy Physics, Chinese Academy of Sciences, Beijing 100049, China*

(Received 26 January 2022; revised 19 May 2022; accepted 20 May 2022; published 14 June 2022)

Generation of arbitrarily spin polarized muon pairs is investigated via polarized e^-e^+ collision. We calculate the completely polarized cross section $d\sigma_{e^-e^+\to\mu^-\mu^+}$ and construct the fully spin-resolved Monte Carlo simulation method to explicitly describe the production of polarized muon pairs. We find that, due to the flip of mixed helicities along the scattering angle, arbitrarily polarized muon pairs with both of the longitudinal and transverse spin components can be produced. Moreover, we also find that the transverse polarization of the muon pairs depends on the directions of transverse spins of initial electrons and positrons. The collision of tightly collimated electron and positron beams with highly longitudinal polarization and nanocoulomb charge can generate about 40% muon pairs with longitudinal polarization and about 60% muon pairs with transverse polarization. The compact high-flux $e^-e^+ \to \mu^-\mu^+$ muon source could be implemented through the next-generation laser-plasma linear collider and would be essential to facilitate the investigation of fundamental physics and the measurement technology in broad areas.

DOI: 10.1103/PhysRevD.105.113002

I. INTRODUCTION

Spin polarized muon sources are versatile in fundamental particle physics, nuclear physics, and condensed matter physics [1–4]. In particle physics, the muon anomalous magnetic moment [5–7], rare muon decay [1,8,9], and muon-neutrino flavor oscillations [10–12] are deemed to encode the experimental evidences in search of the new physics beyond the standard model, demanding the unequivocal measurements by using high-flux polarized muon beams. The longitudinally spin polarized (LSP) and transversely spin polarized (TSP) muon beams can both be used for the precise measurements of the muon anomalous magnetic moment [7] and are crucial for studying the lepton flavor violating [8,13] and the *CP* violation [14,15]. In nuclear physics, the high-flux muon beams apply to the muon-catalyzed fusion [2,16,17], the production of muonic atoms for probing the nuclear properties [18,19], and the muon-capture reaction for producing the nuclear isotope [20]. The LSP muons are used to study the nuclear structure via the polarized deep-inelastic scattering with above 80% polarization [21,22] or via the muon capture with above 70% polarization [23,24]. Moreover, the highly polarized (above 90%) slow muons apply to the muon spin relaxation/rotation (μSR) measurement due to its sensitivity to low spin fluctuation [3,4], whereby the μSR effect is significant in quantum materials, radical chemistry, battery materials, and elemental analysis [25].

The conventional hadronic $\pi^-\pi^+ \to \mu^-\mu^+$ muon source is generated through the proton-nucleon reactions inside a high-Z target, in which the predominantly produced $\pi^\pm$ mesons decay into the polarized muons and, due to the parity nonconservation, these muons are completely longitudinally polarized [26,27]. The TSP muons can be obtained in the storage ring, in which the momenta of LSP muons are deflected by 90° to obtain the TSP ones, however, an integrated field of 492 T m is required in the relativistic limit [28,29]. The hadronic muon source usually demands a kilometer-scale accelerator to obtain the proton-beam driver with energy above 100 MeV, and the muons are required to be efficiently captured and rapidly accelerated from the divergent hadronic showers [26,30].

At present, with the rapid developments of ultraintense, ultrashort laser techniques, the state-of-the-art laser pulses can achieve the peak intensities of about 10^{23} W/cm^2 with a pulse duration of tens of femtoseconds and an energy

*zhaoq2019@xjtu.edu.cn
†jianxing@xjtu.edu.cn

fluctuation of about 1% [31–33]. Efficient laser-driven plasma accelerators with a gradient exceeding 0.1 TeV/m can provide dense tens-of-MeV proton [34,35] and multi-GeV electron beams [36] in experiments, and thus have the potential to significantly accelerate the prepolarized low-energy proton [37–39] and electron beams [40–42]. Moreover, the TSP electron (positron) beam can be directly produced via nonlinear Compton scattering (nonlinear Breit-Wheeler pair production) in an elliptically polarized [43,44] or bichromatic laser pulses [45–48] due to the quantum radiative spin effects, and the LSP ones can be produced via the helicity transfer from circularly polarized γ photons in nonlinear Breit-Wheeler processes [49,50], which are generally preproduced via Compton scattering [51,52] or bremsstrahlung [53]. Very recently, an all-optical spin rotation method has been proposed to generate arbitrarily spin polarized (ASP) lepton and ion beams [54]. Thus, such a strong laser pulse could be used to drive the direct production of muon pairs through the quantum electrodynamics (QED) processes [30], such as the Bethe-Heitler (BH) and trident muon pair productions via the beam-target interaction: $\gamma + Z \to \mu^- + \mu^+ + Z$ and $e^- + Z \to \mu^- + \mu^+ + e^{-'} + Z$, and the triplet and e^-e^+ annihilation muon pair productions via the beam-beam interaction: $e^- + \gamma \to \mu^- + \mu^+ + e^-$ and $e^- + e^+ \to \mu^- + \mu^+$ [55–59]. In the former, the high-brilliance muon beams can be produced through the interaction of a laser-driven GeV electron beam and high-Z target [60]. While, in the latter, the low-emittance ones can be produced through the collisions of a positron beam of about 45 GeV with target electrons [57–59]. However, in these proposals, the polarization of muon pairs are not taken into account. As known, the longitudinal polarization dominates the BH- and tridentlike processes [61]. According to the helicity configure in the $e^-e^+ \to \mu^-\mu^+$ process, in principle, the LSP and TSP muon pairs can both be produced as a transversely polarized state in a linear combination of two helicity states [62]. Thus, it is attractive to examine the prospective ASP muons produced via collisions of the forthcoming polarized electron and positron beams driven by the ultraintense laser.

In this paper, the generation of ASP muon pairs via the polarized e^-e^+ annihilation process has been investigated. We calculate the cross section of muon pair production for ASP scattering particles by virtue of the density matrix (see Sec. II A) and use the fully spin-resolved Monte Carlo (MC) simulation method of binary collision [63] to describe the production and polarization processes of muon pairs (see Sec. II B). The interaction scenario and coordinate system in the momentum space are illustrated in Figs. 1 and 2, respectively. We find that the directions of the initial spins can significantly modify the energy and angular spectra of muons (see Fig. 3). Moreover, we find that the polarized electrons and positrons with opposite helicities annihilate into the polarized muon pairs with mixed helicity states, which flip along the scattering angle

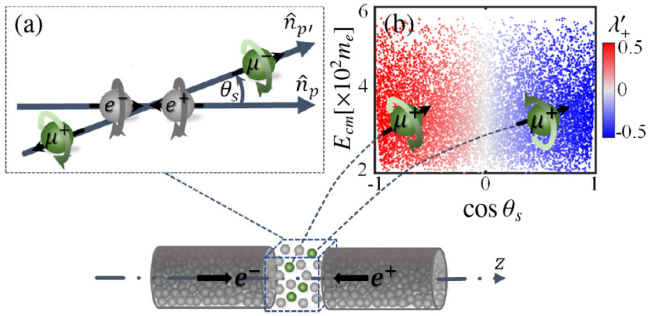

FIG. 1. Interaction scenario for generating ASP muon pairs via polarized e^-e^+ collision. (a) Schematic helicity configuration in the center of mass frame. The black and helical arrows denote the particle momentum direction and mixed helicity, respectively, $\hat{n}_p$ and $\hat{n}_{p'}$ denote the momentum directions of e^- and μ^-, respectively, and θ_s is the scattering angle. (b) Helicity distribution of μ^+ (μ^- has an opposite distribution) in the plane of center of mass energy $E_{\rm cm}$ and $\cos\theta_s$. In our simulation, the electron and positron beams are initialized symmetrically with a transverse Gaussian and longitudinal uniform distribution, divergence angle $\theta_b = 1$ mrad and uniform energy distribution between 110 and 360 MeV in the laboratory frame.

θ_s gradually and lead to the LSP and TSP muon pairs [see Fig. 1(b) and more details in Figs. 4 and 5]. The longitudinal polarization distributes near the colliding axis and the transverse polarization distributes approximately perpendicular to the colliding axis. Utilizing laser-driven LSP electron and positron beams, high-flux ASP muons could be produced directly through an ultrahigh-luminosity laser-plasma collider (see Fig. 6 and Table I), which have significant applications in broad areas.

The paper is organized as follows. Section II summarizes the methods of theory and numerical simulation. Numerical results and related discussions are given in Sec. III. A brief conclusion of this work is presented in Sec. IV.

II. METHODS OF THEORY AND NUMERICAL SIMULATION

The cross section of process $e^-e^+ \to \mu^-\mu^+$ with particle spins can be obtained by introducing a spin projection operator or using a density matrix [64,65]. The polarized

TABLE I. In a symmetric colliding setup with a set of example parameters: charge Q_b, longitudinal size l_z, and transverse size $\sigma_{x/y}$, and repetition frequency $f_{\rm rep}$, the produced muons with total yield $N_{\rm tot}$, and partial yields $N_\parallel$ and $N_\perp$. The electron and positron beams with $P_\parallel^{(e)} = 1$ have the same energy distribution as that in Fig. 6.

Q_b	$(l_z, \sigma_{x/y})$ (μm)	$f_{\rm rep}$ (Hz)	$N_{\rm tot}$	$(N_\parallel, P_\parallel^{(\mu)})$	$(N_\perp, P_\perp^{(\mu)})$
5 nC	(100, 0.3)	10^4	546	(236, 0.79)	(310, 0.83)
500 pC	(50, 0.3)	10^6	591	(257, 0.83)	(334, 0.83)

scattering amplitude of Bhabha scattering and Møller scattering were discussed by considering the initial spins [66,67]. The polarized scattering amplitude considering both initial and final spins can be significantly simplified by applying the helicity eigenstates. However, in general, the produced muon pairs are partially polarized with the energy- and angle-dependent polarization degree. In addition, in order to apply the e^-e^+ annihilation process as a polarized muon source, one should acquire the comprehensive knowledge of the beam effects and polarization characteristics in this leptonic process through the realistic beam-beam collision. Therefore, we calculate the completely polarized cross section using the density matrix (see Sec. II A). Moreover, in order to simulate the beam effects of energy and polarization distributions on the muon pair production and build the bridge between theoretical prediction and experimental procedure, we employ the MC simulation strategy of binary collision [63] (see Sec. II B).

A. Calculation of the fully spin-resolved cross section of the $e^-e^+ \to \mu^-\mu^+$ process

In the calculation of the fully spin-resolved cross section of the muon pair production, we use the Lorentz invariant density matrix to describe the arbitrary polarization (see [63] and Secs. 65 and 87 in [64]). Denoting $\boldsymbol{\zeta}_\pm$ and $\boldsymbol{\zeta}'_\pm$ as mean spin vectors of $e^\pm$ and $\mu^\pm$ (see Sec. 29 in [64]), respectively, whereby the density matrices can be formulated by the defined spin four-vector bases [see Eqs. (9) and (10)]. Defining the Mandelstam invariants in the process $e^-e^+ \to \mu^-\mu^+$ as

$$\begin{aligned} s &= (p_- + p_+)^2 = (p'_- + p'_+)^2; \qquad \tilde{s} = s/m_e^2, \\ t &= (p_- - p'_-)^2 = (p'_+ - p_+)^2; \qquad \tilde{t} = t/m_e^2, \\ u &= (p_- - p'_+)^2 = (p'_- - p_+)^2; \qquad \tilde{u} = u/m_e^2, \end{aligned} \tag{1}$$

where $p_\pm$ and $p'_\pm$ denote the 4-momenta of $e^\pm$ and $\mu^\pm$, respectively. Defining $m = m_\mu/m_e$ with m_e and m_μ being the masses of electron and muon, the obtained cross section in the c.m. frame is

$$\frac{\mathrm{d}\sigma}{\mathrm{d}\Omega} = \frac{r_e^2\sqrt{\tilde{s}-4m^2}|}{64\tilde{s}^3\sqrt{\tilde{s}-4}}|\mathcal{M}|^2, \tag{2}$$

where Ω and r_e are the solid angle and classical radius, respectively. The scattering amplitude $|\mathcal{M}|^2$ is expressed as [64]

$$\begin{aligned} |\mathcal{M}|^2 &= (\bar{v}(p_+,a_+)\gamma^\alpha u(p_-,a_-)\bar{u}(p_-,a_-)\gamma^\beta v(p_+,a_+)) \\ &\quad \times (\bar{u}(p'_-,a'_-)\gamma_\alpha v(p'_+,a'_+)\bar{v}(p'_+,a'_+)\gamma_\beta u(p'_-,a'_-)) \\ &= \mathrm{Tr}^{\mathrm{Dirac}}(\rho_+\gamma^\alpha\rho_-\gamma^\beta)\mathrm{Tr}^{\mathrm{Dirac}}(\rho'_-\gamma_\alpha\rho'_+\gamma_\beta), \end{aligned} \tag{3}$$

where γ_α and γ_β are the gamma matrices, contracted to four-vectors in "slash" notation below, $a_\pm$ and $a'_\pm$ denote the spin four-vectors of $e^\pm$ and $\mu^\pm$, respectively. The density matrices in Eq. (3) are derived from the direct product of the Dirac spinors $u\bar{u}$ and $v\bar{v}$ with the replacements

$$\begin{cases} u(p_-,a_-)\bar{u}(p_-,a_-) \to \rho_-, \\ v(p_+,a_+)\bar{v}(p_+,a_+) \to \rho_+, \\ u(p'_-,a'_-)\bar{u}(p'_-,a'_-) \to \rho'_-, \\ v(p'_+,a'_+)\bar{v}(p'_+,a'_+) \to \rho'_+, \end{cases} \tag{4}$$

with $\rho_\pm = 1/(2m_e)(\not{p}_\pm \mp m_e)[1-\gamma^5(\not{a}_\pm)]$ and $\rho'_\pm = 1/(2m_e)(\not{p}'_\pm \mp m_\mu)[1-\gamma^5(\not{a}'_\pm)]$. The spin four-vectors are expanded as $a_\pm = \sum_{j=1}^3 \zeta_{\pm,j}\hat{e}_j^\pm$ and $a'_\pm = \sum_{j=1}^3 \zeta'_{\pm,j}\hat{u}_j^\pm$, where $\hat{e}^\pm$ and $\hat{u}^\pm$ are the spin four-vector bases of $e^\pm$ and $\mu^\pm$, respectively. Substituting these expansions into the density matrices of $e^\pm$ and $\mu^\pm$, one obtains

$$\begin{cases} \rho_{\pm,0} = 1/(2m_e)(\not{p}_\pm \mp m_e), \\ \rho_{\pm,j} = -\zeta_{\pm,j}\rho_{\pm,0}\gamma_5\not{\hat{e}}_j^\pm, j = 1,2,3, \end{cases} \tag{5}$$

$$\begin{cases} \rho'_{\pm,0} = 1/(2m_e)(\not{p}'_\pm \mp m_\mu), \\ \rho'_{\pm,j} = -\zeta'_{\pm,j}\rho'_{\pm,0}\gamma_5\not{\hat{u}}_j^\pm, j = 1,2,3. \end{cases} \tag{6}$$

Using the momenta of the scattering particles, a set of orthogonal four-vectors

$$\begin{cases} Q = p_- + p_+ = p'_- + p'_+, \\ M = p'_- - p'_+, \\ K_\perp = K - M(p'_-K - p'_+K)/M^2, \\ N = \epsilon^\lambda_{\alpha\beta\rho}Q^\alpha M^\beta K^\rho_\perp, \end{cases} \tag{7}$$

is constructed for defining the spin bases of $e^\pm$, and another set of orthogonal four-vectors

$$\begin{cases} Q = p_- + p_+ = p'_- + p'_+, \\ K = p_- - p_+, \\ M_\perp = M - K(p'_-K - p'_+K)/K^2, \\ L = \epsilon^\lambda_{\alpha\beta\rho}Q^\alpha K^\beta M^\rho_\perp, \end{cases} \tag{8}$$

is constructed for defining the spin bases of $\mu^\pm$. $\epsilon^\lambda_{\alpha\beta\rho}$ is the Levi-Civita tensor. Thus, it is convenient to define the spin four-vector bases for $e^\pm$ with

$$\begin{cases} \hat{e}_0^\pm = p_\pm/m_e, \\ \hat{e}_1^\pm = N/\sqrt{-|N|^2}, \\ \hat{e}_2^\pm = (f_1\cdot p_\pm + f_2\cdot p_\mp)/m_e, \\ \hat{e}_3^\pm = (f_3\cdot M + f_4\cdot K_\perp)/m_e, \end{cases} \tag{9}$$

and for $\mu^\pm$ with

$$\begin{cases} \hat{u}_0^{\pm} = p'_{\pm}/m_\mu, \\ \hat{u}_1^{\pm} = L/\sqrt{-|L|^2}, \\ \hat{u}_2^{\pm} = (f_5 \cdot p'_{\pm} + f_6 \cdot p'_{\mp})/m_e, \\ \hat{u}_3^{\pm} = (f_7 \cdot K + f_8 \cdot M_\perp)/m_e. \end{cases} \tag{10}$$

The coefficients f_1, f_2, f_3, and f_4 are defined by the orthogonal relations between $\hat{e}_2^{\pm}$ and $\hat{e}_3^{\pm}$, and the normalization condition $|\hat{e}_2^{\pm}|^2 = |\hat{e}_3^{\pm}|^2 = -1$. It is similar to the definition of coefficients f_5, f_6, f_7, and f_8 (see Appendix C).

In the c.m. frame, the element of the solid angle is $\mathrm{d}\Omega = \mathrm{d}(-\tilde{t})\mathrm{d}\psi/(2|\boldsymbol{p}||\boldsymbol{p}'|)$, where $\boldsymbol{p}$ and $\boldsymbol{p}'$ being the c.m. momenta of electron and muon, respectively. Substituting Eqs. (5) and (6) into Eq. (3) and calculating the Dirac trace, one obtains the differential cross section of the $e^-e^+ \to \mu^-\mu^+$ process,

$$\frac{\mathrm{d}^2\sigma}{\mathrm{d}\tilde{t}\mathrm{d}\psi} = \frac{r_e^2}{32\tilde{s}^3(\tilde{s}-4)}\left(F + \sum_{i=1}^{3} G_i^- \zeta'_{-,i} + \sum_{i=1}^{3} G_i^+ \zeta'_{+,i} + \sum_{i,j=1}^{3} H_{ij}\zeta'_{-,i}\zeta'_{+,j}\right), \tag{11}$$

where the functions F, $G_i^{\pm}$, and $H_{i,j}$ are expressed by $\tilde{s}, \tilde{t}$, and $\tilde{u}$, and their concrete expressions are presented in Appendix C. ζ'_+ and ζ'_- denote a selecting polarization by a detector and have two spin states, and summing these two spin states of ζ'_+ and ζ'_- in Eq. (11) one obtains

$$\frac{\mathrm{d}^2\bar{\sigma}}{\mathrm{d}\tilde{t}\mathrm{d}\psi} = \frac{r_e^2}{8\tilde{s}^3(\tilde{s}-4)}F. \tag{12}$$

After the integration of Eq. (12) over the azimuth angle ψ and $\tilde{t}$, one obtains the total cross section with the initial spins $\zeta_{\pm,i}$ of $e^{\pm}$

$$\bar{\sigma}_{\mathrm{tot}} = \frac{r_e^2\pi}{4\tilde{s}^3(\tilde{s}-4)}\tilde{F}, \tag{13}$$

where $\tilde{F}$ is the integration of F over $\tilde{t}$ and ψ and is expressed as

$$\begin{aligned}\tilde{F} = {} & \frac{8\sqrt{(\tilde{s}-4)(\tilde{s}-4m^2)}}{3}(4m^2(\tilde{s}+2)+\tilde{s}(2\tilde{s}+4) \\ & + \zeta_{-,1}\zeta_{+,1}(4m^2(\tilde{s}+2)+\tilde{s}(-\tilde{s}+4)) \\ & + \zeta_{-,2}\zeta_{+,2}(4m^2(-\tilde{s}+2)+\tilde{s}(-2\tilde{s}+4)) \\ & + \zeta_{-,3}\zeta_{+,3}(4m^2(-\tilde{s}+2)+\tilde{s}(\tilde{s}+4))).\end{aligned} \tag{14}$$

The obtained cross section (11) as a function of the parameters $\boldsymbol{\zeta}'_{\pm}$ also gives the spin states of $\mu^{\pm}$ resulting from the scattering process itself (see Sec. 65 in [64])

$$\zeta'^{(f)}_{-,j} = \frac{G_j^-}{F}, \qquad \zeta'^{(f)}_{+,j} = \frac{G_j^+}{F}, \quad j = 1,2,3. \tag{15}$$

In the c.m. frame, $\zeta'_{\pm,1}$ and $\zeta_{\pm,1}$ are the transverse polarization perpendicular to the scattering plane, $\zeta'_{\pm,3}$ and $\zeta_{\pm,3}$ are the transverse polarization in the scattering plane, and $\zeta'_{\pm,2}$ and $\zeta_{\pm,2}$ are the longitudinal polarization (see details in Sec. II B). Therefore, the helicity amplitudes can be obtained by setting $\zeta_{\pm,2} = \pm 1$ and $\zeta'_{\pm,2} = \pm 1$ in Eq. (11) as

$$|\mathcal{M}_{+-\pm\mp}|^2 = F \pm G_2^- \mp G_2^+ - H_{22}, \tag{16a}$$

$$|\mathcal{M}_{+-\pm\pm}|^2 = F \pm G_2^- \pm G_2^+ + H_{22}. \tag{16b}$$

The differential cross sections of the four helicity channels $|+-\pm\mp\rangle$ and $|+-\pm\pm\rangle$ are $\mathrm{d}\sigma_{+-\pm\mp}$ and $\mathrm{d}\sigma_{+-\pm\pm}$, respectively, where the subscripts from the first to the fourth in sequence denote the positive ($|+\rangle$) or negative ($|-\rangle$) helicity eigenstates of e^-, e^+, μ^-, and μ^+, respectively. The helicity scattering amplitudes can also be obtained directly by using the helicity states in the calculation of $|\mathcal{M}|^2$ with spin four-vectors $a_{\pm} = \lambda_{\pm}(\frac{|\boldsymbol{p}|}{m_e}, \frac{E_{\pm}}{m_e}\frac{\boldsymbol{p}}{|\boldsymbol{p}|})$ and $a'_{\pm} = \lambda'_{\pm}(\frac{|\boldsymbol{p}'|}{m_\mu}, \frac{E'_{\pm}}{m_\mu}\frac{\boldsymbol{p}'}{|\boldsymbol{p}'|})$, and it is consistent with the deduced ones in Eq. (16) from the arbitrarily-polarized scattering amplitude in Eq. (11).

The spin three-vectors $\boldsymbol{\zeta}'^{(f)}_{\pm}$ can be expressed in an arbitrary frame by the definition of a set of three-vector basis $\boldsymbol{n}'_{\pm}$ [68] as

$$\boldsymbol{\zeta}'^{(f)}_{\pm} = \sum_{j=1}^{3} \zeta'^{(f)}_{\pm,j}\boldsymbol{n}'_{\pm,j}, \tag{17}$$

$$\boldsymbol{n}'_{\pm,j} = \hat{\boldsymbol{u}}_j^{\pm} - \boldsymbol{p}'_{\pm}/(E'_{\pm} + m_\mu)\hat{u}^{\pm}_{j0}, \tag{18}$$

with $\hat{u}^{\pm}_{j0}$ being a time component of four-vector $\hat{u}_j^{\pm}$ defined in Eq. (10), and $E'_{\pm}$ and $\boldsymbol{p}'_{\pm}$ being the energies and momenta of $\mu^{\pm}$ in an arbitrary frame. The three-vector bases $\boldsymbol{n}_{\pm}$ of $e^{\pm}$ can be defined in the same way. Thus, the mean helicities of muon pair in an arbitrary frame are expressed as $\lambda'_{\pm} = \boldsymbol{\zeta}'^{(f)}_{\pm}\boldsymbol{p}'_{\pm}/(2|\boldsymbol{p}'_{\pm}|)$.

B. MC simulation method

Following our developed MC simulation method for polarized binary collision, here, we consider the collision scenarios with realistic electron and positron beams that are initialized with a specific degree of polarization, energy distribution, and divergence angle in the laboratory frame. During the beam-beam collision, the colliding region is meshed into solid cells at every time step, and the electrons that can scatter inside a cell are sampled by Thomson cross section and paired by no-time-count method [69], as

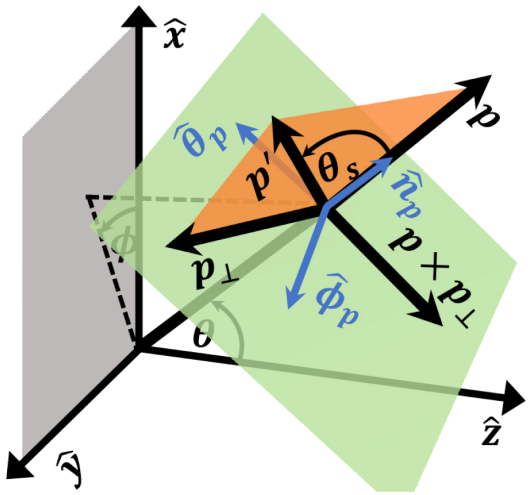

FIG. 2. Coordinate system of the muon pair production in the c.m. frame. θ and ϕ are the polar and azimuth angles of the electron momentum $\boldsymbol{p}$, respectively, and $(\hat{\boldsymbol{n}}_p, \hat{\boldsymbol{\theta}}_p, \hat{\boldsymbol{\phi}}_p)$ are the spherical coordinates of electron momentum $\boldsymbol{p}$. $\boldsymbol{p}_\perp$ in the $\hat{\boldsymbol{\theta}}_p - \hat{\boldsymbol{\phi}}_p$ plane is perpendicular to $\boldsymbol{p}$, and $\boldsymbol{p}'$ in the $\boldsymbol{p} - \boldsymbol{p}_\perp$ plane is the momentum of μ^-.

illustrated in Fig. 1. By the Lorentz boost along the c.m. frame velocity $\boldsymbol{\beta}_{\rm cm}$ $[\boldsymbol{\beta}_{\rm cm} = (\boldsymbol{p}_- + \boldsymbol{p}_+)/(E_- + E_+)$ with momenta $\boldsymbol{p}_\pm$ and energies $E_\pm$ of e^- and e^+ in the laboratory frame], every paired e^-e^+ with $s > 4m_\mu^2$ are permitted for the single annihilation process of muon pair production by using the acceptance-rejection method. For each event, the c.m. momentum $\boldsymbol{p}'$ of muon is determined in the defined momentum coordinate (see Fig. 2), where the scattering angle θ_s is defined as the angle between $\boldsymbol{p}$ and $\boldsymbol{p}'$. With the determined 4-momenta $(E_{\rm cm}, \boldsymbol{p}')$ of a muon pair, one can calculate the transition probabilities of spin states using cross section (11) to determine the final spin state, and the spin axis is also determined by calculating Eq. (18). The detailed architecture of the simulation code is described in Appendix A.

Let us first clarify the determination of muon momenta. Since we calculate the differential cross section Eq. (2) in the c.m. frame, the polar and azimuthal coordinates of a muon in momentum space are defined with respect to the electron momentum $\boldsymbol{p}$. The polar angle of a muon is the scattering angle θ_s in the scattering plane and the azimuthal angle in the azimuthal plane $\hat{\boldsymbol{\theta}}_p - \hat{\boldsymbol{\phi}}_p$, as sketched in Fig. 2. An auxiliary quantity $\boldsymbol{p}_\perp$ (defined in the azimuthal plane by a random angle with respect to $\hat{\boldsymbol{\theta}}_p$) is used to determine $\boldsymbol{p}'$ by the relation $\hat{\boldsymbol{n}}_{p'} = \cos\theta_s \hat{\boldsymbol{n}}_p + \sin\theta_s \hat{\boldsymbol{n}}_{p_\perp}$. The θ_s is obtained by solving $\bar{\sigma}_\theta/\bar{\sigma}_{\rm tot} = |R_1|$, where R_1 is a uniform random number between -1 and 1, and

$$\bar{\sigma}_\theta = \sqrt{(\tilde{s}-4)(\tilde{s}-4m^2)}/2 \int_{-|\cos\theta_s|}^{|\cos\theta_s|} \mathrm{d}\bar{\sigma}, \tag{19}$$

which results in

$$\begin{aligned}\bar{\sigma}_\theta = \sqrt{(\tilde{s}-4)(\tilde{s}-4m^2)}\{&4\tilde{s}|\cos\theta_s|[4m^2(\zeta_{-,1}\zeta_{+,1} - \zeta_{-,2}\zeta_{+,2} \\ &- \zeta_{-,3}\zeta_{+,3} + 1) + \tilde{s}(-\zeta_{-,1}\zeta_{+,1} - \zeta_{-,2}\zeta_{+,2} + \zeta_{-,3}\zeta_{+,3} + 1) \\ &+ 4(\zeta_{-,1}\zeta_{+,1} + 1 + \zeta_{-,2}\zeta_{+,2} + \zeta_{-,3}\zeta_{+,3})] \\ &- \frac{4}{3}|\cos\theta_s|^3(4m^2 - \tilde{s})[\tilde{s}(\zeta_{-,1}\zeta_{+,1} - \zeta_{-,2}\zeta_{+,2} \\ &- \zeta_{-,3}\zeta_{+,3} + 1) - 4(\zeta_{-,1}\zeta_{+,1} + \zeta_{-,2}\zeta_{+,2} + \zeta_{-,3}\zeta_{+,3} + 1)]\}.\end{aligned} \tag{20}$$

In the c.m. frame, the defined spin 3-vector basis in Eq. (18) is concrete, i.e., $(\boldsymbol{n}_{-,1}, \boldsymbol{n}_{-,2}, \boldsymbol{n}_{-,3})$ corresponds to the directions of $(\boldsymbol{p}_\perp \times \boldsymbol{p}, \boldsymbol{p}, -\boldsymbol{p}_\perp)$, and $(\boldsymbol{n}'_{-,1}, \boldsymbol{n}'_{-,2}, \boldsymbol{n}'_{-,3})$ corresponds to the spherical coordinates $(\hat{\boldsymbol{\phi}}_{p'}, \hat{\boldsymbol{n}}_{p'}, \hat{\boldsymbol{\theta}}_{p'})$ of $\boldsymbol{p}'$, respectively, as shown in Fig. 2. Therefore, in the c.m. frame, a muon is produced in each single reaction with the longitudinal polarization $\zeta'^{(f)}_{-,2}$ and the transverse polarization $\zeta'^{(f)}_{-,1}$ and $\zeta'^{(f)}_{-,3}$ along $\hat{\boldsymbol{\phi}}_{p'}$ and $\hat{\boldsymbol{\theta}}_{p'}$, respectively. We denote $\zeta'_\parallel$ and $\zeta'_\perp$ as the longitudinal and transverse polarizations of μ^-, respectively, namely

$$\zeta'_\parallel \equiv \zeta'^{(f)}_{-,2}, \qquad \zeta'_\perp \equiv \sqrt{(\zeta'^{(f)}_{-,1})^2 + (\zeta'^{(f)}_{-,3})^2}. \tag{21}$$

Thus, the energy- and angle-dependent polarization can be analytically obtained by Eq. (15). Alternatively, $\zeta'_\parallel$ is the difference between counting rates for positive and negative helicities [summed over polarization states $\pm\boldsymbol{\zeta}'_+$ $(\pm\boldsymbol{\zeta}'_-)$ of μ^+], normalized to the total counting rate,

$$\zeta'_\parallel = \frac{\sum_{\boldsymbol{\zeta}'_+}[\mathrm{d}\sigma(\zeta'_{-,2} = 1) - \mathrm{d}\sigma(\zeta'_{-,2} = -1)]}{\sum_{\boldsymbol{\zeta}'_+}[\mathrm{d}\sigma(\zeta'_{-,2} = 1) + \mathrm{d}\sigma(\zeta'_{-,2} = -1)]}, \tag{22}$$

and it is similar to obtain the expression of $\zeta'_\perp$ from the counting rates.

Although the characteristic distribution of polarization in the phase space ($E_{\rm cm} - \theta_s$ space) can be obtained analytical by Eq. (21), it is necessary to know the single spin state of each pair in order to acquire the statistical polarization of the produced muon pairs. The single spin state can be determined by the MC sampling using the corresponding transition probabilities given in Eq. (11). The statistical meaning of the mean polarization of a single muon is that in a piece of the phase space, the distributed mean polarization can be retrieved by the observed spin components averaged over particle number. The observed spin states of $\mu^\pm$ are determined by the following four transition probabilities:

$$W^{\uparrow\uparrow} = \int \mathrm{d}\Omega[0.25 + \boldsymbol{\zeta}'^{(f)}_{+}\boldsymbol{\zeta}^{(d)}_{+} + \boldsymbol{\zeta}'^{(f)}_{-}\boldsymbol{\zeta}^{(d)}_{-} + (\boldsymbol{\zeta}^{(d)}_{-})^{T} H \boldsymbol{\zeta}^{(d)}_{+}], \tag{23a}$$

$$W^{\uparrow\downarrow} = \int \mathrm{d}\Omega[0.25 + \boldsymbol{\zeta}'^{(f)}_{+}\boldsymbol{\zeta}^{(d)}_{+} - \boldsymbol{\zeta}'^{(f)}_{-}\boldsymbol{\zeta}^{(d)}_{-} - (\boldsymbol{\zeta}^{(d)}_{-})^{T} H \boldsymbol{\zeta}^{(d)}_{+}], \tag{23b}$$

$$W^{\downarrow\uparrow} = \int \mathrm{d}\Omega[0.25 - \boldsymbol{\zeta}'^{(f)}_{+}\boldsymbol{\zeta}^{(d)}_{+} + \boldsymbol{\zeta}'^{(f)}_{-}\boldsymbol{\zeta}^{(d)}_{-} - (\boldsymbol{\zeta}^{(d)}_{-})^{T} H \boldsymbol{\zeta}^{(d)}_{+}], \tag{23c}$$

$$W^{\downarrow\downarrow} = \int \mathrm{d}\Omega[0.25 - \boldsymbol{\zeta}'^{(f)}_{+}\boldsymbol{\zeta}^{(d)}_{+} - \boldsymbol{\zeta}'^{(f)}_{-}\boldsymbol{\zeta}^{(d)}_{-} + (\boldsymbol{\zeta}^{(d)}_{-})^{T} H \boldsymbol{\zeta}^{(d)}_{+}]. \tag{23d}$$

Each of them consists of the spin-projecting terms (the second and third terms in square brackets) and correlation term (the fourth term in square brackets) between $\boldsymbol{\zeta}'^{(f)}_{\pm}$ and the spin axis $\pm\boldsymbol{\zeta}^{(d)}_{\pm}$ (unit vector) of a detector. Each transition probability determines the signs of the observed spin components $\zeta^{(d)}_{\pm,i} = \zeta'^{(f)}_{\pm,i}/|\boldsymbol{\zeta}'^{(f)}_{\pm}|$ $(i = 1, 2, 3)$, namely, the parallel or antiparallel projection onto the spin axis. Thus we can employ the MC sampling by a uniform random number $0 < R_2 < 1$ as follows:

(i) $R_2 \in (0, W^{\uparrow\uparrow})$ results in $+\zeta^{(d)}_{+,i}, +\zeta^{(d)}_{-,i}$;
(ii) $R_2 \in (W^{\uparrow\uparrow}, W^{\downarrow\downarrow} + W^{\uparrow\uparrow})$ results in $-\zeta^{(d)}_{+,i}, -\zeta^{(d)}_{-,i}$;
(iii) $R_2 \in (W^{\downarrow\downarrow} + W^{\uparrow\uparrow}, W^{\uparrow\downarrow} + W^{\downarrow\downarrow} + W^{\uparrow\uparrow})$ results in $+\zeta^{(d)}_{+,i}, -\zeta^{(d)}_{-,i}$;
(iv) $R_2 \in (W^{\uparrow\downarrow} + W^{\downarrow\downarrow} + W^{\uparrow\uparrow}, 1)$ results in $-\zeta^{(d)}_{+,i}, +\zeta^{(d)}_{-,i}$.

Defining $\boldsymbol{\zeta}^{(d)}_{\pm}$ along the directions of $\boldsymbol{\zeta}'^{(f)}_{\pm}$ leads to the statistical polarization of produced $\mu^{\pm}$ beams

$$P^{(\mu)}_{\mathrm{tot}} = \sqrt{(\bar{\zeta}^{(d)}_{\pm,1})^2 + (\bar{\zeta}^{(d)}_{\pm,2})^2 + (\bar{\zeta}^{(d)}_{\pm,3})^2}, \tag{24}$$

with the averaged components $\bar{\zeta}^{(d)}_{\pm,i}$ over the particle number, and $P^{(\mu)}_{\mathrm{tot}}$ is the total polarization. If one defines $\boldsymbol{\zeta}^{(d)}_{\pm}$ as the parallel or perpendicular directions of the $\mu^{\pm}$ momenta, one obtains the statistical beam polarization with the longitudinal ($P^{(\mu)}_{\parallel}$) or transverse components ($P^{(\mu)}_{\perp}$). Similarly, we denote $P^{(e)}_{\parallel}$ and $P^{(e)}_{\perp}$ as the longitudinal and transverse polarizations of electron (positron) beams.

In the simulations, we consider that the energy distribution in the given electron and positron beams is spatially homogeneous and defined by a characteristic constant, then the muon yield in a single collision N_{sc} can be written as [70]

$$N_{sc} = \iiiint \frac{\mathrm{d}n_{\mu}}{\mathrm{d}\tau}\mathrm{d}^3V\mathrm{d}\tau = \mathcal{L}_{e^-e^+} \times \bar{\sigma}^{\mathrm{int}}_{\mathrm{tot}}, \tag{25}$$

in terms of the single collision geometric luminosity $\mathcal{L}_{e^-e^+}$ of the beam-beam collision [71], where d^3V and $\mathrm{d}\tau$ are the infinitesimal volume and time, respectively, and an integrated cross section $\bar{\sigma}^{\mathrm{int}}_{\mathrm{tot}}$ is obtained by coupling the energy distribution functions of electron and positron beams to the total cross section $\bar{\sigma}_{\mathrm{tot}}$. In our simulation, instead of $\mathcal{L}_{e^-e^+}$, which measures the ability of a collider producing the required number of interactions, the e^-e^+ collisions are sampled by the Thomson cross section σ_T, which leads to the maximum number of collision N_{max} (see Appendix A). Thus, the muon yield can also be estimated as

$$N_{sc} = \frac{N_{\mathrm{max}}}{\sigma_T} \times \bar{\sigma}^{\mathrm{int}}_{\mathrm{tot}}. \tag{26}$$

In the simulation, the energy-coupled $\bar{\sigma}^{\mathrm{int}}_{\mathrm{tot}}$ is consistently considered into each single muon pair production. N_{max} in Eq. (26) is sampled by Thomson cross section and proportional to beam density. For electron and positron beams with specific parameters, considering multiple beam-beam collisions with repetition frequency f_{rep}, the total muon yield is thus estimated as $N_{\mathrm{tot}} = f_{\mathrm{rep}}N_{sc}$, in which the quantity $f_{\mathrm{rep}}N_{\mathrm{max}}$ can be interpreted as the equivalent maximum number N^*_{max} resulted from an equivalent single collision of beams with an equivalent charge Q^*_b.

III. SIMULATION RESULTS AND DISCUSSIONS

In this section, we first present the impact of initial spins of $e^{\pm}$ on the cross section with summarized final spins (see Fig. 3), then, the polarization mechanism in the muon pair production is analyzed via the helicity amplitudes (see Figs. 4 and 5). Finally, by varying the initial polarization of electron and positron beams, the polarization curves of the muon beams are obtained (see Fig. 6), and the feasible beam parameters for producing the required polarized muon pairs are examined (see Table I).

As known, the annihilation process $e^-e^+ \to \gamma\gamma$ and elastic scattering process $e^-e^+ \to e^-e^+$ also occur in the e^-e^+ collision, and the corresponding total cross sections are shown in Fig. 3(a). These three processes are competitive in a single collision, and the annihilation process is the most probable reaction. In the simulation, these three processes are considered into the rejection procedure simultaneously, the γ-photon yield produced in the annihilation process is more than 10 times larger than the muon pair yield, and this difference is consistent with that between the cross sections (see the comparison in Appendix A). The influence of the elastic scattering process on the initial polarization of electron and positron beams is negligible due to the smallest cross section $\bar{\sigma}_{e^-e^+\to e^-e^+}$.

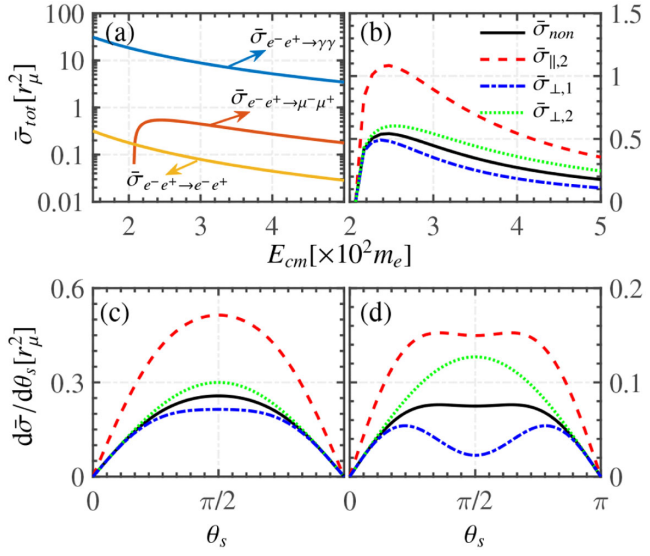

FIG. 3. (a) The total cross sections of three processes in the e^-e^+ interaction. (b) $\bar{\sigma}_{\rm tot}$ vs $E_{\rm cm}$ calculated from Eq. (13) with four initial spin states: nonpolarized $\bar{\sigma}_{\rm non}$, LSP $\bar{\sigma}_{\parallel,2}$ with $\zeta_{-,2}\zeta_{+,2}=-1$, and TSP $\bar{\sigma}_{\perp,1}$ and $\bar{\sigma}_{\perp,2}$ with $\zeta_{-,1}\zeta_{+,1}=1$ and $\zeta_{-,1}\zeta_{+,1}=-1$, respectively. (c),(d) The differential cross sections vs θ_s at the peak energies E_p and $2E_p$, respectively. The line types in (c) and (d) have the same meanings as those in (b) but for $d\bar{\sigma}_{\rm non}/d\theta_s$, $d\bar{\sigma}_{\parallel,2}/d\theta_s$, $d\bar{\sigma}_{\perp,1}/d\theta_s$, and $d\bar{\sigma}_{\perp,2}/d\theta_s$ calculated from Eq. (12). The unit of the cross section here and below is r_μ^2 with $r_\mu = r_e/m$.

The effects of initial spin states of $e^\pm$ on the spin-summarized cross section of the muon pair production are shown in Figs. 3(b)–3(d). Here one has $\bar{\sigma}_{\rm non}=(\bar{\sigma}_{\parallel,1}+\bar{\sigma}_{\parallel,2})/2=(\bar{\sigma}_{\perp,1}+\bar{\sigma}_{\perp,2})/2$. Note that the

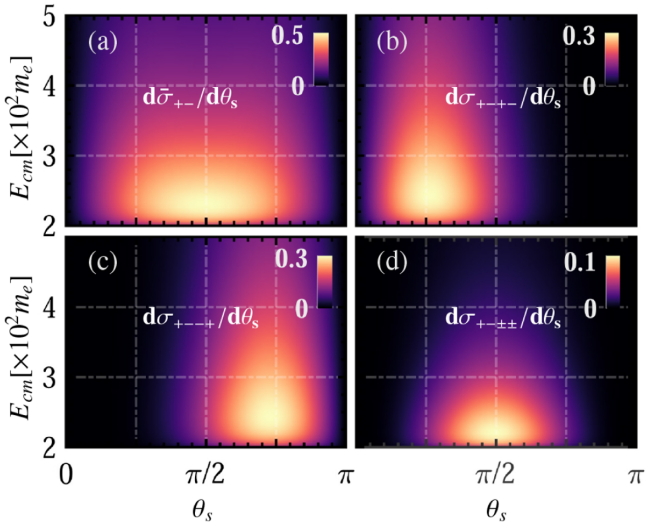

FIG. 4. Distributions of differential cross section in the plane of θ_s and $E_{\rm cm}$: (a) with summarized final spins $d\bar{\sigma}_{+-}/d\theta_s$ [calculated via Eq. (12)], and (b)–(d) with different helicity channels [calculated via Eq. (16)].

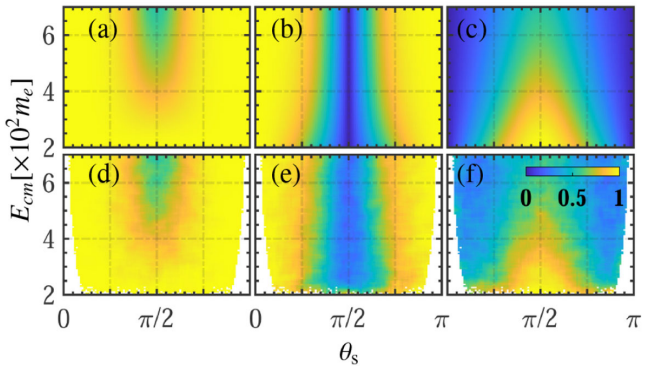

FIG. 5. Polarization distributions in the plane of θ_s and $E_{\rm cm}$ are produced by $e_R^- e_L^+$ collision with helicity eigenstates: (a)–(c) corresponding to ζ', $\zeta'_\parallel$, and $\zeta'_\perp$, respectively, calculated by Eq. (15) or Eq. (22); (d)–(f) corresponding to corresponding to $P_{\rm tot}^{(\mu)}$, $P_\parallel^{(\mu)}$, and $P_\perp^{(\mu)}$, respectively, calculated by Eq. (24) via MC simulations. The simulation parameters are the same as those in Fig. 1.

component $\bar{\sigma}_{\parallel,1}$ with $\zeta_{-,2}\zeta_{+,2}=1$ equals zero because the corresponding helicity channel leads to the nonexistent virtual photon state and is forbidden. Therefore, $\bar{\sigma}_{\parallel,2}$ is twice $\bar{\sigma}_{\rm non}$ [see Fig. 3(b)]. For the spin-summarized differential cross section, its distribution with respect to θ_s presents the different energy dependence for different spin states of $e^\pm$. As $E_{\rm cm}$ increases, $d\bar{\sigma}_{\rm non}/d\theta_s$ and $d\bar{\sigma}_{\parallel,2}/d\theta_s$

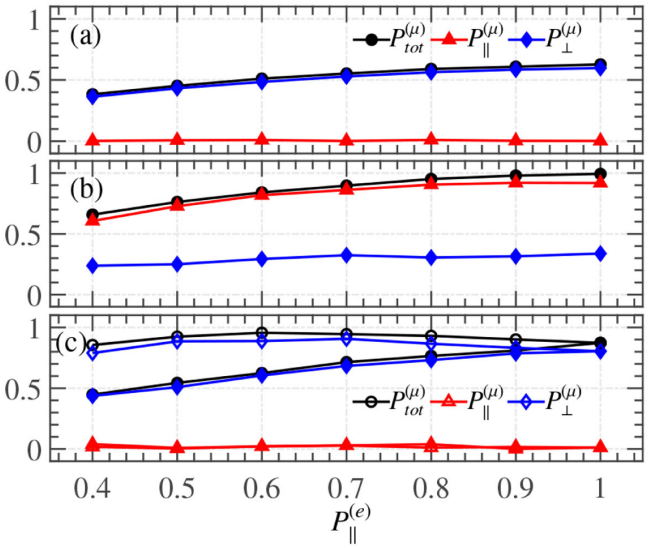

FIG. 6. (a)–(c) Polarization of muons vs $P_\parallel^{(e)}$ for all the muons, the muons beamed into $0<\theta<0.2\pi$ and $0.3\pi<\theta<0.7\pi$, respectively. The filled marks denote the results produced from the collisions with antiparallel transverse polarization $\zeta_{+,\perp}=-\zeta_{-,\perp}$, and the hollow marks in (c) denote the results produced from the collisions with parallel transverse polarization $\zeta_{+,\perp}=\zeta_{-,\perp}$. Other parameters are the same as those in Fig. 1 but having an exponential energy distribution with an average energy $E_{av}=125$ MeV in the laboratory frame.

vary from the cosine angular spectra to the flattop angular spectra, and the cosine-shaped $d\bar{\sigma}_{\perp,2}/d\theta_s$ increases against decreasing $d\bar{\sigma}_{\perp,1}/d\theta_s$ with two peaks [see Figs. 3(c) and 3(d)]. Therefore, the collisions of electrons and positrons with opposite helicities can produce polarized muons with higher yield compared with other polarization configurations. In the following, without loss of generality we focus on the processes of muon-pair production via the collisions of electrons with right-handed helicity (denoted as e_R^-) and positrons with left-handed helicity (denoted as e_L^+).

Considering the spins of the muon pair in Eq. (11) with arbitrary $\boldsymbol{\zeta}'_+$ and $\boldsymbol{\zeta}'_-$, the polarization of muons with mixed spin states can be clarified through the cross sections of helicity channels. The distributed mean helicities of muon pairs originate from the linear superpositions of four helicity channels with weights determined by $d\sigma_{+-\pm\mp}/d\bar{\sigma}_{+-}$ and $d\sigma_{+-\pm\pm}/d\bar{\sigma}_{+-}$. The distributions of the cross sections of four helicity channels are shown in Fig. 4. As shown in Figs. 4(b) and 4(c), the asymmetric distributions of $d\sigma_{+-+-}/d\theta_s$ and $d\sigma_{+---}/d\theta_s$ indicate the helicity flip along θ_s, i.e., λ'_+ varies from -0.5 to 0.5 for $0 < \theta_s < \pi$ (a reverse variation for λ'_-) [see Fig. 1(b)]. Consequently, $|+-+-\rangle$ and $|+--+\rangle$ channels contribute to the longitudinal polarization of muon pairs, and the degree of longitudinal polarization is calculated by Eq. (22). Differently, the distributions of $d\sigma_{+-++}/d\theta_s$ and $d\sigma_{+---}/d\theta_s$ are completely overlapping and symmetric along θ_s [see Fig. 4(d)]. As a result, $|+-++\rangle$ and $|+---\rangle$ channels lead to the equal-weight linear superposition between helicity states $|+\rangle$ and $|-\rangle$, and thus contribute to the purely transverse polarization [62]. Note that the spin-correlated term in Eq. (11) has non-negligible contribution to the cross sections of $|+-\pm\pm\rangle$ channels and, subsequently, to the transverse polarization.

The helicity distributions determine the polarization characteristics of produced muons. For the e^-e^+ collision with opposite helicity eigenstates, the distributions of the total polarization and its LSP and TSP components are shown in Fig. 5. $\zeta'_\parallel$ only originates from $|+-+-\rangle$ and $|+--+\rangle$ channels, and substituting the cross sections of these two channels [see Fig. 4] into Eq. (22), one obtains the symmetric distribution of $\zeta'_\parallel$ along θ_s for muon pairs [equivalent to the calculation of Eq. (21)], as shown in Fig. 5(b). While the distributed $\zeta'_\perp$ originates from both the four channels, $|+-++\rangle$ and $|+---\rangle$ channels contribute the pure transverse polarization around $\theta_s = \pi/2$, and the partially overlapping cross sections of $|+-+-\rangle$ and $|+--+\rangle$ channels lead to the nonequal weights of $\mu^\pm$ at the helicity states $|\pm\rangle$ and, subsequently, the partially transverse polarization [see Fig. 5(c)]. For the realistic beam-beam collision, our MC simulation results of polarization distributions (reactions are forbidden along $\theta_s = 0$ and π) are consistent well with the analytical calculations [see Figs. 5(d)–5(f)], which manifests the statistical meaning of $\zeta'_\parallel$ and $\zeta'_\perp$ in Eq. (21). According to these characteristic distributions of polarization, in the $e_R^-e_L^+$ collisions, the LSP muons can be extracted from the region of $\theta_s \lesssim 0.3\pi$ or $\theta_s \gtrsim 0.7\pi$, and the TSP muons can be extracted from the region of $0.3\pi \lesssim \theta_s \lesssim 0.7\pi$. The polarization distributions of muons from partially LSP electron and positron beams are also revealed and presented in Fig. 8 in Appendix B.

In order to illustrate the polarization transfer efficiency from the polarized electron (positron) beam, the latter is initialized with varying $P_\parallel^{(e)}$ and $P_\perp^{(e)}$ but maintaining $(P_\parallel^{(e)})^2 + (P_\perp^{(e)})^2 = 1$. The resulted polarization curves vs $P_\parallel^{(e)}$ are shown in Fig. 6. Because the $e_R^-e_L^+$ collisions lead to the canceled mean helicities besides $\theta_s = \pi/2$, the statistical $P_\parallel^{(\mu)}$ is vanished for all the produced muons, and thus $P_{\rm tot}^{(\mu)} = P_\perp^{(\mu)}$ and increases linearly with $P_\parallel^{(e)}$ [see Fig. 6(a)]. The LSP muons can be extracted from the paraxial region where $P_\parallel^{(\mu)}$ dominates the polarization due to the final spin state $|+-\rangle$ or $|-+\rangle$ [see Fig. 6(b)]. Note that both $P_\perp^{(e)} = 0$ and nonzero $P_\perp^{(e)}$ with $\boldsymbol{\zeta}_{+,\perp} = \boldsymbol{\zeta}_{-,\perp}$ result in the similar polarization curves as those in see Fig. 6(b). The TSP muons are scattered around $\theta = \pi/2$, and the polarization curves of $P_\perp^{(\mu)}$ are distinguished between the $e_R^-e_L^+$ collisions with mutually antiparallel and parallel transverse spin components. The antiparallel case with $\boldsymbol{\zeta}_{+,\perp} = -\boldsymbol{\zeta}_{-,\perp}$ leads to the linear growth of $P_\perp^{(\mu)}$, which is equivalent to the case $P_\perp^{(e)} = 0$, while the parallel case with $\boldsymbol{\zeta}_{+,\perp} = \boldsymbol{\zeta}_{-,\perp}$ leads to the approximately flat variation of $P_\perp^{(\mu)}$ [see Fig. 6(c)]. The main reason is that, for the latter case, the cross section with final helicity states $|\pm\pm\rangle$ is an order of magnitude larger than that for the former case, and thus has larger contribution to $P_\perp^{(\mu)}$ at higher energy and smaller $P_\parallel^{(e)}$ (see detailed presentations in Fig. 9 in Appendix B). The reactions between the polarized electron beam and nonpolarized positron beam (or vice versa) also produce the similar polarization curve to Fig. 6 but with the half-reduced yield.

The muon yields produced from a symmetric colliding setup with specific beams are shown in Table I, where $f_{\rm rep}$ is estimated by the colliding beams with an equivalent 500 nC charge (see the explanation in Sec. II B). The results indicate that about 40% LSP muon pairs ($\theta \lesssim 0.3\pi$ and $\theta \gtrsim 0.7\pi$) and about 60% TSP muon pairs ($0.3\pi \lesssim \theta \lesssim 0.7\pi$) with approximate 80% polarization degree are produced in the assumed colliding setup. The higher degree of polarization with approximate 90% for LSP and TSP muons can be filtered by the narrower regions of θ (see Fig. 6). Moreover, the beam-beam collision can be designed as a charge-asymmetric setup, namely, with a nanocoulomb electron beam and a

hundreds-of-picocoulomb positron beam, which can significantly reduce the beam disruption at the interaction point [72]. Furthermore, the emittance of produced muons can be reduced by the tunable energy asymmetry of tens of MeV between electron and positron beams. However, we find that the polarized muons cannot be produced in the colliding electron and positron beams with a GeV energy asymmetry due to the vanished average spin components, thus the interaction of a positron beam and target electrons cannot generate the polarized muon source [57–59].

The implement of the leptonic $e^-e^+ \to \mu^-\mu^+$ muon source depends on the high-luminosity e^-e^+ collisions. As an advanced next-generation collider, the laser-plasma-accelerator-based linear e^-e^+ colliders have attracted broad interest recently due to their compact scale [73–76]. The theoretical calculations assess that, by virtue of the kilohertz laser pulse, the laser-driven wakefield sustains the multibunch beams with continuous transverse focusing to produce a nanometer beam size, which permits the laser-plasma linear collider to operate at very high luminosity on the order of 10^{34} cm^{-2} s^{-1} [74,75]. We underline that the dense electron beams with tens of nanocoulomb charge and hundreds of MeV energy can be generated through the direct laser acceleration [77,78] or laser-wakefield acceleration [79,80]. The interaction of laser-wakefield electron beams with high-Z target induces the production of the positron shower with tens of nanocoulomb charge and the energy exceeding 100 MeV [81,82], which could be trapped and accelerated as a high-quality beam in the laser (beam) wakefield [83–85]. Thus the laser-driven electron and positron beams with ultrahigh charge afford the ultrahigh-luminosity laser-plasma linear collider for the generation of $e^-e^+ \to \mu^-\mu^+$ muon source.

IV. CONCLUSION

In summary, we investigate the generation of ASP muon pairs via the collision of polarized electron and positron beams. We calculate the cross section of process $e^- + e^+ \to \mu^- + \mu^+$ with arbitrary spins of four leptons and develop the fully spin-resolved MC method to simulate the polarized muon-pair productions in the realistic beam-beam collision. Both the LSP and TSP muon pairs can be produced simultaneously in the $e_R^- e_L^+$ collisions and are beamed into regions around parallel and perpendicular directions of the colliding axis, respectively. The polarization mechanism of the muon-pair production is clarified through the differential cross section with different helicity channels. Our calculations indicate that, based on the current platform of laser-plasma acceleration, it has potential to generate LSP electron and positron beams with the charge from hundreds of picocoulomb to tens of nanocoulomb, which could promise to produce ASP muon pairs via the ultrahigh-luminosity laser-plasma collider scheme. Our proposed leptonic muon source could be applicable in broad areas, such as laser-plasma, nuclear, high-energy particle, and condensed matter physics.

ACKNOWLEDGMENTS

This work is supported by the National Natural Science Foundation of China (Grants No. 12022506, No. 11874295, No. 11875219, No. 11655003, No. 11905169, No. 12105217), the China Postdoctoral Science Foundation (Grant No. 2020M683447), the Innovation Project of IHEP (No. 542017IHEPZZBS11820, No. 542018IHEPZZBS12427), and the CAS Center for Excellence in Particle Physics (CCEPP).

APPENDIX A: NUMERICAL SIMULATION METHOD

In the simulations, the realistic e^- and e^+ (not macroparticles) are randomized with energy and spatial distributions. Following the algorithm in [69], we consider a collision cell containing N_- electrons in the beam (1) and N_+ positrons in the beam (2), the maximum probability of a collision within a unit time Δt and a unit volume ΔV is

$$P_{\max} = 2\sigma_T c \Delta\tau / \Delta V, \tag{A1}$$

where σ_T is the Thomson cross section and used as the reference cross section. At each colliding time step, the maximal number of e^- and e^+ in a cell that are probable to scatter is $N_{\max} = P_{\max} N_- N_+$. After randomly sorting the particles of each beam in a cell, the e^- and e^+ used to be paired for collision are selected from the first $N_{\max}$ particles in each sorted e^- or e^+ list. The event probability is given by

$$P^{i,j} = (\bar{\sigma}_{\text{tot}} c \Delta\tau / \Delta V) / P_{\max}. \tag{A2}$$

The collision of a paired $e^\pm$ is admitted to the $\mu^\pm$ pair production process based on a rejection method, i.e., for a random number R_0, accept if $P^{i,j} > R_0$.

If we consider the competitive one-order QED processes in each e^-e^+ collision: $e^-e^+ \to \gamma\gamma$, $e^-e^+ \to \mu^-\mu^+$, and $e^-e^+ \to e^-e^+$, the event is determined by the selection method. We define $P_{\gamma\gamma} = \bar{\sigma}_{e^-e^+\to\gamma\gamma}/2\sigma_T$, $P_{\mu^-\mu^+} = \bar{\sigma}_{e^-e^+\to\mu^-\mu^+}/2\sigma_T$, and $P_{e^-e^+} = \bar{\sigma}_{e^-e^+\to e^-e^+}/2\sigma_T$. Randomize a uniform number R_0 between 0 and 1 and execute the following selections:

(i) $R_0 \in (0, P_{\gamma\gamma})$ leads to the annihilation process;
(ii) $R_0 \in (P_{\gamma\gamma}, P_{\mu^-\mu^+} + P_{\gamma\gamma})$ leads to the muon-pair production process;
(iii) $R_0 \in (P_{\mu^-\mu^+} + P_{\gamma\gamma}, P_{e^-e^+} + P_{\mu^-\mu^+} + P_{\gamma\gamma})$ leads to the elastic scattering process;
(iv) $R_0 \in (P_{e^-e^+} + P_{\mu^-\mu^+} + P_{\gamma\gamma}, 1)$ leads to no reaction.

The production yield of these three processes in the collision of e^- and e^+ beams is shown in Fig. 7(a).

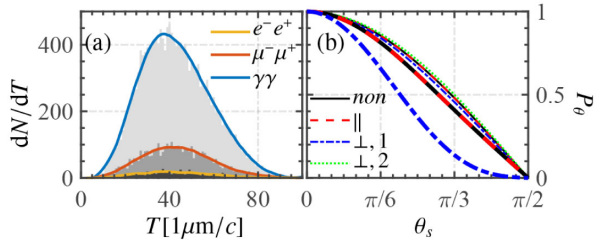

FIG. 7. (a) Reaction rates of three different processes in the collision of e^- and e^+ beams. (b) $P_\theta = \bar{\sigma}_\theta/\bar{\sigma}_{\rm tot}$ vs θ_s for nonpolarized (non), LSP (∥). and TSP (⊥) $e^\pm$, calculated from Eqs. (13) and (20), where the line types have the same meanings as Fig. 3(b). The thin and thick lines correspond to $E_{\rm cm} =$ 125 MeV and 1 GeV, respectively.

With the definition $P_\theta = \bar{\sigma}_\theta/\bar{\sigma}_{\rm tot}$, the distribution of P_θ implies that the produced pair is scattered into $d\theta_s$ with a corresponding probability dP_θ, as shown in Fig. 7(b). Figure 7(b) also indicates the energy-independent profile of P_θ for the "⊥, 2" case (the thin, green dotted and thick, green dotted lines are overlapping), which leads to the reaction forbiddance near $\theta_s = 0$ or $\theta_s = \pi$ as the corresponding dP_θ equals zero. Thus, θ_s can be determined solving the equation $P_\theta(\theta_s) = R_1$ via MC sampling, where R_1 is a uniform random number between −1 and 1. After the determination of θ_s, the momenta of $\mu^\pm$ in the c.m. frame can be determined according to the momentum relations presented in Fig. 2. The energy and momentum of muons in the laboratory frame are also calculated by the Lorentz transformation

$$\gamma'_\pm = \gamma'\gamma_{\rm cm}(1 \mp \boldsymbol{\beta}^2_{\rm cm}\boldsymbol{\beta}')\cos\theta_u, \tag{A3}$$

$$\boldsymbol{p}'_\pm = \left(\boldsymbol{p}' \mp \frac{(\gamma_{\rm cm}-1)}{\beta^2_{\rm cm}}\beta'\gamma'\cos\theta_u\boldsymbol{\beta}_{\rm cm}\right) \mp \frac{\gamma_{\rm cm}}{\beta'}\boldsymbol{\beta}_{\rm cm}, \tag{A4}$$

where $\gamma_{\rm cm} = 1/\sqrt{1-\beta^2_{\rm cm}}$ and $\gamma'\beta' = |\boldsymbol{p}'|$. θ_u is the angle between $\boldsymbol{\beta}_{\rm cm}$ and $\boldsymbol{p}'$. With the determined momenta, the degree of polarization can be calculated analytically from Eqs. (21) and (24) through MC simulation.

Finally, the execution of the simulation code is performed as follows:

(i) Initialize the $e^\pm$ beams with an energy distribution, angle divergence and mean spin.
(ii) Grid the collision region into 3D cells at simulation time T_1.
(iii) Pare the colliding $e^\pm$ inside the first cell $\Delta x_1\Delta y_1\Delta z_1$ using the no-time-count method and transform each pair from the laboratory from to the c.m. frame.
(iv) Randomize a number R_0 and use the rejection method to generate $\mu^\pm$ pairs inside the cell. If $P^{i,j}$ is too large (say, >0.1), divide the interval $\Delta\tau$ (and $P^{i,j}$) by an integer $N_{\rm div}$, and repeat the following procedure $N_{\rm div}$ times.
(v) Randomize another number R_1 between −1 and 1 to determine the scattering angle θ_s and hence the momenta of the created pair in the c.m. frame.
(vi) Calculate Eqs. (15) and (18) by the determined momenta, and randomize a number R_2 to determine the observable spin state.
(vii) Go back to step 3 and undertake the next paired collision of $e^\pm$.

APPENDIX B: THE DISTRIBUTION OF POLARIZATION PRODUCED FROM PARTIALLY POLARIZED ELECTRONS AND POSITRONS

For the $e^-_R e^+_L$ collision with partially polarized electron and positron beams, the distributions of $P^{(\mu)}_{\rm tot}$, $P^{(\mu)}_\parallel$ and $P^{(\mu)}_\perp$ are shown in Fig. 8. The structures of the distributed polarization are not changed, but, as $P^{(e)}_\parallel$ decreases, the polarization magnitudes decrease as well. Thus we say that the polarization structure is determined by the final helicity channels and the magnitudes of the polarization is determined by the initial polarization degree.

The influences of initially transverse spins on the distributions of polarization are shown in Fig. 9. For the $e^-_R e^+_L$ collision with the mutually antiparallel transverse spins, i.e., $\boldsymbol{\zeta}_{+,\perp} = -\boldsymbol{\zeta}_{-,\perp}$, the reactions are almost forbidden in the regions of $\theta_s \lesssim 0.1\pi$ and $\theta_s \gtrsim 0.9\pi$ [see Figs. 9(e) and 9(f)], because of the energy-independent change of P_θ [see green dotted line Fig. 7(b)]. While for the $e^-_R e^+_L$ collision with the mutually parallel transverse spins, i.e., $\boldsymbol{\zeta}_{+,\perp} = \boldsymbol{\zeta}_{-,\perp}$, the distribution of $P^{(\mu)}_\parallel$ approaches the one from the $e^-_R e^+_L$ collision without transverse

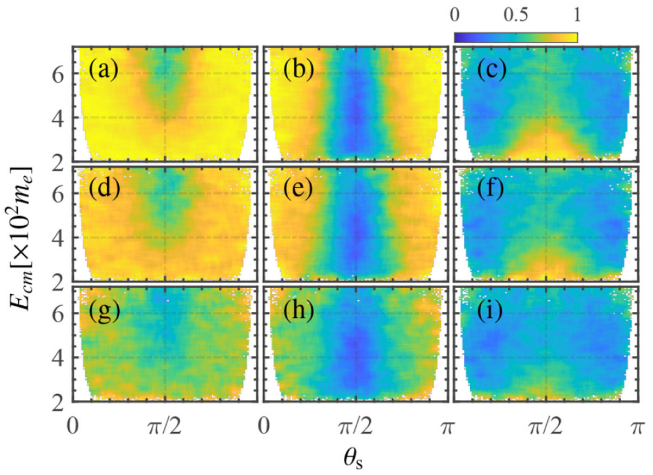

FIG. 8. Polarization distributions of (a),(d),(g) $P^{(\mu)}_{\rm tot}$, (b),(e),(h) $P^{(\mu)}_\parallel$, and (c),(f),(i) $P^{(\mu)}_\perp$, produced by colliding electron and positron beams with (a)–(c) $P^{(e)}_\parallel = 0.8$, (d)–(f) $P^{(e)}_\parallel = 0.6$, and (g)–(i) $P^{(e)}_\parallel = 0.4$, respectively. There is no transverse polarization of initial beams.

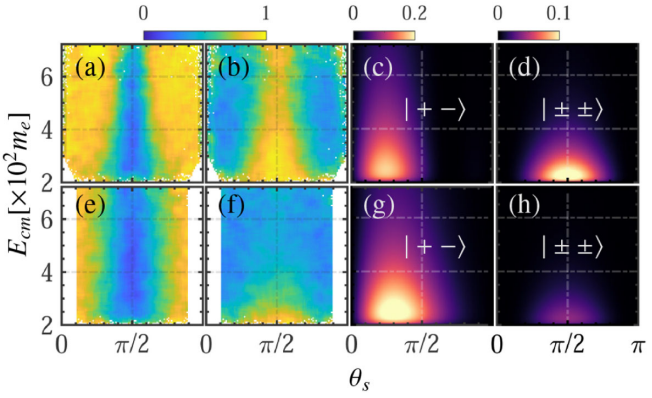

FIG. 9. Distributions of simulated polarization. (a) $P_{\parallel}^{(\mu)}$ and (b) $P_{\perp}^{(\mu)}$, produced from $e_R^- e_L^+$ collisions with $P_{\parallel}^{(e)} = 0.6$ and parallel transverse polarization $\boldsymbol{\zeta}_{+,\perp} = \boldsymbol{\zeta}_{-,\perp}$, together with the corresponding differential cross sections with final helicity states: (c) $|+-\rangle$ and (d) $|\pm\pm\rangle$. (e)–(h) are similar to (a)–(d) but for $e_R^- e_L^+$ collisions with antiparallel transverse polarization $\boldsymbol{\zeta}_{+,\perp} = -\boldsymbol{\zeta}_{-,\perp}$.

polarization [see Figs. 8(e) and 9(a)]. Additionally, the distribution of $P_{\perp}^{(\mu)}$ near $\theta_s = \pi/2$ remains remarkable as the energy increases [see Fig. 9(b)], because the $|\pm\pm\rangle$ components of cross section with $\boldsymbol{\zeta}_{+,\perp} = \boldsymbol{\zeta}_{-,\perp}$ are larger than those with $\boldsymbol{\zeta}_{+,\perp} = -\boldsymbol{\zeta}_{-,\perp}$ by an order of magnitude [see Figs. 9(d) and 9(h)].

APPENDIX C: THE EXPRESSIONS OF COEFFICIENTS IN EQS. (9)–(11)

The coefficients f_1, f_2, f_3, and f_4 in Eq. (9) are

$$f_1 = \frac{\tilde{s}/2 - 1}{\sqrt{(\tilde{s}/2-1)^2 - 1}}, \tag{C1a}$$

$$f_2 = -\frac{1}{\sqrt{(\tilde{s}/2-1)^2 - 1}}, \tag{C1b}$$

$$f_3 = \frac{-((\tilde{t}-\tilde{u})^2/(4m^2-\tilde{s}) + \tilde{s} - 4)}{\sqrt{(\tilde{s}-4)((\tilde{s}-4)(\tilde{s}-4m^2) - (\tilde{t}-\tilde{u})^2)}}, \tag{C1c}$$

$$f_4 = \frac{\tilde{t}-\tilde{u}}{\sqrt{(\tilde{s}-4)((\tilde{s}-4)(\tilde{s}-4m^2) - (\tilde{t}-\tilde{u})^2)}}. \tag{C1d}$$

The coefficients f_5, f_6, f_7, and f_8 in Eq. (10) are

$$f_5 = \frac{\tilde{s}/2 - m^2}{\sqrt{-(m^4\tilde{s} - \tilde{s}^2 m^2/4)}}, \tag{C2a}$$

$$f_6 = -\frac{m^2}{\sqrt{-(m^4\tilde{s} - \tilde{s}^2 m^2/4)}}, \tag{C2b}$$

$$f_7 = \frac{\sqrt{2(2m^2 - \tilde{s}/2 - (\tilde{t}-\tilde{u})^2/(8-2\tilde{s}))}}{\sqrt{(4-\tilde{s})(\tilde{s}-4m^2)}}, \tag{C2c}$$

$$f_8 = -\frac{(\tilde{t}-\tilde{u})\sqrt{(2m^2 - \tilde{s}/2 - (\tilde{t}-\tilde{u})^2/(8-2\tilde{s}))}}{(-2m^2 + \tilde{s}/2 + (\tilde{t}-\tilde{u})^2/(8-2\tilde{s}))\sqrt{2(4-\tilde{s})(\tilde{s}-4m^2)}}. \tag{C2d}$$

The final-state spin irrelevant term is

$$\begin{aligned}
F = {} & \frac{1}{(\tilde{s}-4)^2} 8(-2m^4(\tilde{s}-4)^2(\zeta_{-,1}\zeta_{+,1} + \zeta_{-,2}\zeta_{+,2} - \zeta_{-,3}\zeta_{+,3} - 1) + 2(-(\tilde{s}-4)\zeta_{-,2}\zeta_{+,3}\tilde{t}\sqrt{-\tilde{s}(4m^2(\tilde{s}-4) - \tilde{s}^2 + 4\tilde{s} + (\tilde{t}-\tilde{u})^2)} \\
& + (\tilde{s}-4)\zeta_{-,2}\zeta_{+,3}\tilde{u}\sqrt{-\tilde{s}(4m^2(\tilde{s}-4) - \tilde{s}^2 + 4\tilde{s} + (\tilde{t}-\tilde{u})^2)} + (\tilde{s}-4)\zeta_{+,2}\zeta_{-,3}\tilde{t}\sqrt{-\tilde{s}(4m^2(\tilde{s}-4) - \tilde{s}^2 + 4\tilde{s} + (\tilde{t}-\tilde{u})^2)} \\
& - (\tilde{s}-4)\zeta_{+,2}\zeta_{-,3}\tilde{u}\sqrt{-\tilde{s}(4m^2(\tilde{s}-4) - \tilde{s}^2 + 4\tilde{s} + (\tilde{t}-\tilde{u})^2)} - 16\zeta_{-,1}\zeta_{+,1}\tilde{t}\tilde{u} + 16\zeta_{-,1}\zeta_{+,1}\tilde{t} + 16\zeta_{-,1}\zeta_{+,1}\tilde{u} - 16\zeta_{-,1}\zeta_{+,1} \\
& - 16\zeta_{-,2}\zeta_{+,2}\tilde{t}\tilde{u} + 16\zeta_{-,2}\zeta_{+,2}\tilde{t} + 16\zeta_{-,2}\zeta_{+,2}\tilde{u} - 16\zeta_{-,2}\zeta_{+,2} + 8\zeta_{-,3}\zeta_{+,3}\tilde{t}^2 - 16\zeta_{-,3}\zeta_{+,3}\tilde{t} + 8\zeta_{-,3}\zeta_{+,3}\tilde{u}^2 - 16\zeta_{-,3}\zeta_{+,3}\tilde{u} \\
& + 16\zeta_{-,3}\zeta_{+,3} + 8\tilde{t}^2 - 16\tilde{t} + 8\tilde{u}^2 - 16\tilde{u} + 16) + 2m^2(\tilde{s}-4)^2(\tilde{s}(\zeta_{-,1}\zeta_{+,1} - \zeta_{-,2}\zeta_{+,2} - \zeta_{-,3}\zeta_{+,3} + 1) \\
& + (\tilde{t}+\tilde{u}-2)(\zeta_{-,1}\zeta_{+,1} + \zeta_{-,2}\zeta_{+,2} - \zeta_{-,3}\zeta_{+,3} - 1)) + 2\tilde{s}^3(\zeta_{-,1}\zeta_{+,1} + \zeta_{-,2}\zeta_{+,2} + \zeta_{-,3}\zeta_{+,3} + 1) - \tilde{s}^2(2\tilde{t}(\zeta_{-,1}\zeta_{+,1}(\tilde{u}-1) \\
& - \zeta_{-,2}\zeta_{+,2} - \zeta_{-,3}\zeta_{+,3}\tilde{u} + \zeta_{-,3}\zeta_{+,3} + 1) - 2\tilde{u}(\zeta_{-,1}\zeta_{+,1} + \zeta_{-,2}\zeta_{+,2} - \zeta_{-,3}\zeta_{+,3} - 1) + 2(9\zeta_{-,1}\zeta_{+,1} + 9\zeta_{-,2}\zeta_{+,2} + 7\zeta_{-,3}\zeta_{+,3} + 7) \\
& + \tilde{t}^2(\zeta_{-,2}\zeta_{+,2} - 1) + \tilde{u}^2(\zeta_{-,2}\zeta_{+,2} - 1)) + 4\tilde{s}(2\tilde{t}(2\zeta_{-,1}\zeta_{+,1}(\tilde{u}-1) + \zeta_{-,2}\zeta_{+,2}(\tilde{u}-2) - \zeta_{-,3}\zeta_{+,3}\tilde{u} + 2\zeta_{-,3}\zeta_{+,3} + 2) \\
& - 4\tilde{u}(\zeta_{-,1}\zeta_{+,1} + \zeta_{-,2}\zeta_{+,2} - \zeta_{-,3}\zeta_{+,3} - 1) + 4(3\zeta_{-,1}\zeta_{+,1} + 3\zeta_{-,2}\zeta_{+,2} + \zeta_{-,3}\zeta_{+,3} + 1) + \tilde{t}^2(\zeta_{-,2}\zeta_{+,2} - \zeta_{-,3}\zeta_{+,3} - 2) \\
& + \tilde{u}^2(\zeta_{-,2}\zeta_{+,2} - \zeta_{-,3}\zeta_{+,3} - 2))).
\end{aligned} \tag{C3}$$

The coefficients of $\zeta'_{-,i}$ are

$$G_1^- = -32m(\zeta_{-,1}+\zeta_{+,1})(2m^2-\tilde{t}-\tilde{u}+2), \tag{C4a}$$

$$G_2^- = -\frac{1}{m(\tilde{s}-4)(4m^2-\tilde{s})}8\sqrt{m^2\tilde{s}(\tilde{s}-4m^2)}(2m^2-\tilde{t}-\tilde{u}+2)(-2(\zeta_{-,3}+\zeta_{+,3})\sqrt{-(4m^2(\tilde{s}-4)-\tilde{s}^2+4\tilde{s}+(\tilde{t}-\tilde{u})^2)}$$
$$\times\sqrt{(\tilde{s}-4)}+\sqrt{(\tilde{s}-4)\tilde{s}}\tilde{t}(\zeta_{-,2}-\zeta_{+,2})-\sqrt{(\tilde{s}-4)\tilde{s}}\tilde{u}(\zeta_{-,2}-\zeta_{+,2})), \tag{C4b}$$

$$G_3^- = (16m(2m^2-\tilde{t}-\tilde{u}+2)((\tilde{t}-\tilde{u})(-2(\zeta_{-,3}+\zeta_{+,3})\sqrt{-(\tilde{s}-4)(4m^2(\tilde{s}-4)-\tilde{s}^2+4\tilde{s}+(\tilde{t}-\tilde{u})^2)}$$
$$+\sqrt{(\tilde{s}-4)\tilde{s}}\tilde{t}(\zeta_{-,2}-\zeta_{+,2})-\sqrt{(\tilde{s}-4)\tilde{s}}\tilde{u}(\zeta_{-,2}-\zeta_{+,2}))+4m^2(\tilde{s}-4)\sqrt{(\tilde{s}-4)\tilde{s}}(\zeta_{-,2}-\zeta_{+,2})-\tilde{s}^2\sqrt{(\tilde{s}-4)\tilde{s}}(\zeta_{-,2}-\zeta_{+,2})$$
$$+4\tilde{s}\sqrt{(\tilde{s}-4)\tilde{s}}(\zeta_{-,2}-\zeta_{+,2})))/\left((\tilde{s}-4)\sqrt{(\tilde{s}-4)(4m^2-\tilde{s})}\sqrt{\frac{4m^2(\tilde{s}-4)-\tilde{s}^2+4\tilde{s}+(\tilde{t}-\tilde{u})^2}{\tilde{s}-4}}\right). \tag{C4c}$$

The coefficients of $\zeta'_{+,i}$ are

$$G_1^+ = -32m(\zeta_{-,1}+\zeta_{+,1})(2m^2-\tilde{t}-\tilde{u}+2), \tag{C5a}$$

$$G_2^+ = \frac{1}{m(\tilde{s}-4)(4m^2-\tilde{s})}8\sqrt{m^2\tilde{s}(\tilde{s}-4m^2)}(2m^2-\tilde{t}-\tilde{u}+2)(-2(\zeta_{-,3}+\zeta_{+,3})\sqrt{-(4m^2(\tilde{s}-4)-\tilde{s}^2+4\tilde{s}+(\tilde{t}-\tilde{u})^2)}$$
$$\times\sqrt{(\tilde{s}-4)}+\sqrt{(\tilde{s}-4)\tilde{s}}\tilde{t}(\zeta_{-,2}-\zeta_{+,2})-\sqrt{(\tilde{s}-4)\tilde{s}}\tilde{u}(\zeta_{-,2}-\zeta_{+,2})), \tag{C5b}$$

$$G_3^+ = (16m(2m^2-\tilde{t}-\tilde{u}+2)((\tilde{t}-\tilde{u})(-2(\zeta_{-,3}+\zeta_{+,3})\sqrt{-(\tilde{s}-4)(4m^2(\tilde{s}-4)-\tilde{s}^2+4\tilde{s}+(\tilde{t}-\tilde{u})^2)}+\sqrt{(\tilde{s}-4)\tilde{s}}\tilde{t}(\zeta_{-,2}-\zeta_{+,2})$$
$$-\sqrt{(\tilde{s}-4)\tilde{s}}\tilde{u}(\zeta_{-,2}-\zeta_{+,2}))+4m^2(\tilde{s}-4)\sqrt{(\tilde{s}-4)\tilde{s}}(\zeta_{-,2}-\zeta_{+,2})-\tilde{s}^2\sqrt{(\tilde{s}-4)\tilde{s}}(\zeta_{-,2}-\zeta_{+,2})$$
$$+4\tilde{s}\sqrt{(\tilde{s}-4)\tilde{s}}(\zeta_{-,2}-\zeta_{+,2})))/\left((\tilde{s}-4)\sqrt{(\tilde{s}-4)(4m^2-\tilde{s})}\sqrt{\frac{4m^2(\tilde{s}-4)-\tilde{s}^2+4\tilde{s}+(\tilde{t}-\tilde{u})^2}{\tilde{s}-4}}\right). \tag{C5c}$$

The coefficients of $\zeta'_{-,i}\zeta'_{+,j}$ are

$$H_{11} = \frac{1}{(\tilde{s}-4)^2\tilde{s}}8(2m^4(\tilde{s}-4)^2(\tilde{s}(\zeta_{-,1}\zeta_{+,1}-\zeta_{-,2}\zeta_{+,2}-\zeta_{-,3}\zeta_{+,3}+1)+4(\zeta_{-,1}\zeta_{+,1}+\zeta_{-,2}\zeta_{+,2}+\zeta_{-,3}\zeta_{+,3}+1))-2\tilde{s}(\tilde{t}(\sqrt{\tilde{s}}$$
$$\times(\tilde{s}-4)\zeta_{-,2}\zeta_{+,3}\sqrt{-(4m^2(\tilde{s}-4)-\tilde{s}^2+4\tilde{s}+(\tilde{t}-\tilde{u})^2)}-(\tilde{s}-4)\zeta_{+,2}\zeta_{-,3}\sqrt{-\tilde{s}(4m^2(\tilde{s}-4)-\tilde{s}^2+4\tilde{s}+(\tilde{t}-\tilde{u})^2)}$$
$$+16\zeta_{-,1}\zeta_{+,1}\tilde{u}-16\zeta_{-,1}\zeta_{+,1}+32\zeta_{-,2}\zeta_{+,2}\tilde{u}-48\zeta_{-,2}\zeta_{+,2}+32\zeta_{-,3}\zeta_{+,3}\tilde{u}-48\zeta_{-,3}\zeta_{+,3}+16\tilde{u}-16)-\tilde{u}(\sqrt{(\tilde{s}-4)\tilde{s}}$$
$$\times\zeta_{-,2}\zeta_{+,3}\sqrt{-(\tilde{s}-4)(4m^2(\tilde{s}-4)-\tilde{s}^2+4\tilde{s}+(\tilde{t}-\tilde{u})^2)}-(\tilde{s}-4)\zeta_{+,2}\zeta_{-,3}\sqrt{-\tilde{s}(4m^2(\tilde{s}-4)-\tilde{s}^2+4\tilde{s}+(\tilde{t}-\tilde{u})^2)}$$
$$+16\zeta_{-,1}\zeta_{+,1}+48\zeta_{-,2}\zeta_{+,2}+48\zeta_{-,3}\zeta_{+,3}+16)+16(\zeta_{-,1}\zeta_{+,1}+3\zeta_{-,2}\zeta_{+,2}+3\zeta_{-,3}\zeta_{+,3}+1)+8\tilde{t}^2(\zeta_{-,2}\zeta_{+,2}+\zeta_{-,3}\zeta_{+,3})$$
$$+8\tilde{u}^2(\zeta_{-,2}\zeta_{+,2}+\zeta_{-,3}\zeta_{+,3}))+2m^2(\tilde{s}-4)^2(\tilde{s}^2(\zeta_{-,1}\zeta_{+,1}-\zeta_{-,2}\zeta_{+,2}-\zeta_{-,3}\zeta_{+,3}+1)-\tilde{s}(\tilde{t}+\tilde{u}-2)(\zeta_{-,1}\zeta_{+,1}-\zeta_{-,2}\zeta_{+,2}$$
$$-\zeta_{-,3}\zeta_{+,3}+1)-4(\tilde{t}+\tilde{u}-2)(\zeta_{-,1}\zeta_{+,1}+\zeta_{-,2}\zeta_{+,2}+\zeta_{-,3}\zeta_{+,3}+1))+\tilde{s}^5(\zeta_{-,2}\zeta_{+,2}-1)+\tilde{s}^4(8-8\zeta_{-,2}\zeta_{+,2})+\tilde{s}^3(\tilde{t}^2(\zeta_{-,1}\zeta_{+,1}$$
$$-\zeta_{-,2}\zeta_{+,2}-\zeta_{-,3}\zeta_{+,3}+1)+\tilde{t}(-2\zeta_{-,1}\zeta_{+,1}+2\zeta_{-,2}\zeta_{+,2}+2\zeta_{-,3}\zeta_{+,3}-2)+\tilde{u}^2(\zeta_{-,1}\zeta_{+,1}-\zeta_{-,2}\zeta_{+,2}-\zeta_{-,3}\zeta_{+,3}+1)$$
$$+\tilde{u}(-2\zeta_{-,1}\zeta_{+,1}+2\zeta_{-,2}\zeta_{+,2}+2\zeta_{-,3}\zeta_{+,3}-2)+2(\zeta_{-,1}\zeta_{+,1}+7\zeta_{-,2}\zeta_{+,2}-\zeta_{-,3}\zeta_{+,3}-7))+\tilde{s}^2(\tilde{t}^2(-6\zeta_{-,1}\zeta_{+,1}+6\zeta_{-,2}\zeta_{+,2}$$
$$+6\zeta_{-,3}\zeta_{+,3}-6)+4\tilde{t}(\tilde{u}(\zeta_{-,1}\zeta_{+,1}+3\zeta_{-,2}\zeta_{+,2}+3\zeta_{-,3}\zeta_{+,3}+1)+2\zeta_{-,1}\zeta_{+,1}-6\zeta_{-,2}\zeta_{+,2}-6\zeta_{-,3}\zeta_{+,3}+2)+\tilde{u}^2(-6\zeta_{-,1}\zeta_{+,1}$$
$$+6\zeta_{-,2}\zeta_{+,2}+6\zeta_{-,3}\zeta_{+,3}-6)+8\tilde{u}(\zeta_{-,1}\zeta_{+,1}-3\zeta_{-,2}\zeta_{+,2}-3\zeta_{-,3}\zeta_{+,3}+1)-8(\zeta_{-,1}\zeta_{+,1}-3\zeta_{-,2}\zeta_{+,2}-3\zeta_{-,3}\zeta_{+,3}+1))$$
$$+32(\tilde{t}+\tilde{u}-2)^2(\zeta_{-,1}\zeta_{+,1}+\zeta_{-,2}\zeta_{+,2}+\zeta_{-,3}\zeta_{+,3}+1)), \tag{C6a}$$

$$H_{12} = -\frac{1}{((\tilde{s}-4)\tilde{s})^{3/2}\sqrt{m^2\tilde{s}(\tilde{s}-4m^2)}}32m^2\tilde{s}^3(-2m^2\tilde{s}\zeta_{-,1}\zeta_{+,2} - (\tilde{s}-4)\zeta_{+,1}\zeta_{-,2}(-2m^2+\tilde{s}+2\tilde{t}-2) + 8m^2\zeta_{-,1}\zeta_{+,2}$$
$$+ (\tilde{s}-4)\zeta_{-,1}\zeta_{+,3}\sqrt{-\tilde{s}(m^4-2m^2(\tilde{t}+1)+(\tilde{s}-2)\tilde{t}+\tilde{t}^2+1)}$$
$$+ (\tilde{s}-4)\zeta_{+,1}\zeta_{-,3}\sqrt{-\tilde{s}(m^4-2m^2(\tilde{t}+1)+(\tilde{s}-2)\tilde{t}+\tilde{t}^2+1)}$$
$$+ \tilde{s}^2\zeta_{-,1}\zeta_{+,2} + 2\tilde{s}\zeta_{-,1}\zeta_{+,2}\tilde{t} - 6\tilde{s}\zeta_{-,1}\zeta_{+,2} - 8\zeta_{-,1}\zeta_{+,2}\tilde{t} + 8\zeta_{-,1}\zeta_{+,2}), \tag{C6b}$$

$$H_{13} = (8\tilde{s}(\tilde{s}^2\sqrt{-(\tilde{s}-4)(m^4-2m^2(\tilde{t}+1)+(\tilde{s}-2)\tilde{t}+\tilde{t}^2+1)}(\zeta_{-,1}\zeta_{+,3}+\zeta_{+,1}\zeta_{-,3}) - 2\tilde{s}(-\zeta_{-,1}\tilde{t}(\zeta_{+,3}\sqrt{(\tilde{s}-4)}$$
$$\times\sqrt{-(m^4-2m^2(\tilde{t}+1)+(\tilde{s}-2)\tilde{t}+\tilde{t}^2+1)} + 2\sqrt{(\tilde{s}-4)\tilde{s}}\zeta_{+,2}) + (m^2+1)\zeta_{-,1}\zeta_{+,3}\sqrt{(\tilde{s}-4)}$$
$$\times\sqrt{-(m^4-2m^2(\tilde{t}+1)+(\tilde{s}-2)\tilde{t}+\tilde{t}^2+1)} + \zeta_{+,1}\zeta_{-,3}(m^2-\tilde{t}+1)\sqrt{-(\tilde{s}-4)(m^4-2m^2(\tilde{t}+1)+(\tilde{s}-2)\tilde{t}+\tilde{t}^2+1)})$$
$$+ 4\sqrt{(\tilde{s}-4)\tilde{s}}\zeta_{-,1}\zeta_{+,2}(m^4-2m^2(\tilde{t}+1)+(\tilde{t}-1)^2) - 4\sqrt{(\tilde{s}-4)\tilde{s}}\zeta_{+,1}\zeta_{-,2}(m^4-2m^2(\tilde{t}+1)$$
$$+ (\tilde{s}-2)\tilde{t}+\tilde{t}^2+1)))/((\tilde{s}-4)\sqrt{m^4-2m^2(\tilde{t}+1)+(\tilde{s}-2)\tilde{t}+\tilde{t}^2+1}\sqrt{(4m^2-\tilde{s})}), \tag{C6c}$$

$$H_{21} = \frac{1}{((\tilde{s}-4)\tilde{s})^{3/2}\sqrt{m^2\tilde{s}(\tilde{s}-4m^2)}}32m^2\tilde{s}^3(-2m^2\tilde{s}\zeta_{-,1}\zeta_{+,2} - (\tilde{s}-4)\zeta_{+,1}\zeta_{-,2}(-2m^2+\tilde{s}+2\tilde{t}-2) + 8m^2\zeta_{-,1}\zeta_{+,2}$$
$$+ (\tilde{s}-4)\zeta_{-,1}\zeta_{+,3}\sqrt{-\tilde{s}(m^4-2m^2(\tilde{t}+1)+(\tilde{s}-2)\tilde{t}+\tilde{t}^2+1)} + (\tilde{s}-4)\zeta_{+,1}\zeta_{-,3}\sqrt{-\tilde{s}(m^4-2m^2(\tilde{t}+1)+(\tilde{s}-2)\tilde{t}+\tilde{t}^2+1)}$$
$$+ \tilde{s}^2\zeta_{-,1}\zeta_{+,2} + 2\tilde{s}\zeta_{-,1}\zeta_{+,2}\tilde{t} - 6\tilde{s}\zeta_{-,1}\zeta_{+,2} - 8\zeta_{-,1}\zeta_{+,2}\tilde{t} + 8\zeta_{-,1}\zeta_{+,2}), \tag{C6d}$$

$$H_{22} = \frac{1}{(\tilde{s}-4)^2(4m^2-\tilde{s})}8(8(\tilde{s}-4)^2(\zeta_{-,1}\zeta_{+,1}+\zeta_{-,2}\zeta_{+,2}-\zeta_{-,3}\zeta_{+,3}-1)m^6 + 2(\tilde{s}-4)^2(\tilde{s}(3\zeta_{-,1}\zeta_{+,1}-5\zeta_{-,2}\zeta_{+,2}-3\zeta_{-,3}\zeta_{+,3}+5)$$
$$-4(\tilde{t}+\tilde{u}-2)(\zeta_{-,1}\zeta_{+,1}+\zeta_{-,2}\zeta_{+,2}-\zeta_{-,3}\zeta_{+,3}-1))m^4 - 2((\zeta_{-,1}\zeta_{+,1}-\zeta_{-,2}\zeta_{+,2}-\zeta_{-,3}\zeta_{+,3}+1)\tilde{s}^4 + (-\zeta_{-,1}\zeta_{+,1}\tilde{u}-\zeta_{-,2}\zeta_{+,2}\tilde{u}$$
$$+\zeta_{-,3}\zeta_{+,3}\tilde{u}+\tilde{u}-2\zeta_{-,1}\zeta_{+,1}+14\zeta_{-,2}\zeta_{+,2}+10\zeta_{-,3}\zeta_{+,3}+\tilde{t}(-\zeta_{-,1}\zeta_{+,1}-\zeta_{-,2}\zeta_{+,2}+\zeta_{-,3}\zeta_{+,3}+1)-6)\tilde{s}^3$$
$$-2((\zeta_{-,1}\zeta_{+,1}-\zeta_{-,3}\zeta_{+,3})\tilde{t}^2 + 2(-3\zeta_{-,1}\zeta_{+,1}-3\zeta_{-,2}\zeta_{+,2}+\tilde{u}(\zeta_{-,2}\zeta_{+,2}-1)+3\zeta_{-,3}\zeta_{+,3}+3)\tilde{t}+\tilde{u}^2(\zeta_{-,1}\zeta_{+,1}-\zeta_{-,3}\zeta_{+,3})$$
$$-6\tilde{u}(\zeta_{-,1}\zeta_{+,1}+\zeta_{-,2}\zeta_{+,2}-\zeta_{-,3}\zeta_{+,3}-1)+2(9\zeta_{-,1}\zeta_{+,1}+17\zeta_{-,2}\zeta_{+,2}+7\zeta_{-,3}\zeta_{+,3}-1))\tilde{s}^2$$
$$+8((2\zeta_{-,1}\zeta_{+,1}+\zeta_{-,2}\zeta_{+,2}-\zeta_{-,3}\zeta_{+,3})\tilde{t}^2 + 2(-3\zeta_{-,1}\zeta_{+,1}-3\zeta_{-,2}\zeta_{+,2}+3\zeta_{-,3}\zeta_{+,3}$$
$$+\tilde{u}(\zeta_{-,2}\zeta_{+,2}-\zeta_{-,3}\zeta_{+,3}-2)+3)\tilde{t}+16(\zeta_{-,1}\zeta_{+,1}+\zeta_{-,2}\zeta_{+,2})-6\tilde{u}(\zeta_{-,1}\zeta_{+,1}+\zeta_{-,2}\zeta_{+,2}-\zeta_{-,3}\zeta_{+,3}-1)$$
$$+\tilde{u}^2(2\zeta_{-,1}\zeta_{+,1}+\zeta_{-,2}\zeta_{+,2}-\zeta_{-,3}\zeta_{+,3}))\tilde{s} - 4(8\zeta_{-,1}\zeta_{+,1}\tilde{t}^2+8\zeta_{-,2}\zeta_{+,2}\tilde{t}^2-16\tilde{t}\tilde{u}-16\zeta_{-,1}\zeta_{+,1}\tilde{t}-16\zeta_{-,2}\zeta_{+,2}\tilde{t}$$
$$+(\tilde{s}-4)\sqrt{-\tilde{s}(4m^2(\tilde{s}-4)-\tilde{s}^2+4\tilde{s}+(\tilde{t}-\tilde{u})^2)}\zeta_{-,3}\zeta_{+,2}\tilde{t} - (\tilde{s}-4)\sqrt{-\tilde{s}(4m^2(\tilde{s}-4)-\tilde{s}^2+4\tilde{s}+(\tilde{t}-\tilde{u})^2)}\zeta_{-,2}\zeta_{+,3}\tilde{t}$$
$$-16\tilde{u}\zeta_{-,3}\zeta_{+,3}\tilde{t}+16\zeta_{-,3}\zeta_{+,3}\tilde{t}+16\tilde{t}+16\tilde{u}+8\tilde{u}^2\zeta_{-,1}\zeta_{+,1}-16\tilde{u}\zeta_{-,1}\zeta_{+,1}+16\zeta_{-,1}\zeta_{+,1}+8\tilde{u}^2\zeta_{-,2}\zeta_{+,2}-16\tilde{u}\zeta_{-,2}\zeta_{+,2}$$
$$+16\zeta_{-,2}\zeta_{+,2}-\sqrt{-\tilde{s}(4m^2(\tilde{s}-4)-\tilde{s}^2+4\tilde{s}+(\tilde{t}-\tilde{u})^2)}(\tilde{s}-4)\tilde{u}\zeta_{-,3}\zeta_{+,2}$$

$$
\begin{aligned}
&+\sqrt{-\tilde{s}(4m^2(\tilde{s}-4)-\tilde{s}^2+4\tilde{s}+(\tilde{t}-\tilde{u})^2)}(\tilde{s}-4)\tilde{u}\zeta_{-,2}\zeta_{+,3}+16\tilde{u}\zeta_{-,3}\zeta_{+,3}-16\zeta_{-,3}\zeta_{+,3}-16))m^2\\
&+\tilde{s}(2(\zeta_{-,1}\zeta_{+,1}+\zeta_{-,2}\zeta_{+,2}+\zeta_{-,3}\zeta_{+,3}+1)\tilde{s}^3-((\zeta_{-,2}\zeta_{+,2}-1)\tilde{t}^2+2((\tilde{u}-1)\zeta_{-,1}\zeta_{+,1}-\zeta_{-,2}\zeta_{+,2}-\tilde{u}\zeta_{-,3}\zeta_{+,3}+\zeta_{-,3}\zeta_{+,3}+1)\tilde{t}\\
&+\tilde{u}^2(\zeta_{-,2}\zeta_{+,2}-1)-2\tilde{u}(\zeta_{-,1}\zeta_{+,1}+\zeta_{-,2}\zeta_{+,2}-\zeta_{-,3}\zeta_{+,3}-1)+2(9\zeta_{-,1}\zeta_{+,1}+9\zeta_{-,2}\zeta_{+,2}+7\zeta_{-,3}\zeta_{+,3}+7))\tilde{s}^2\\
&+4((\zeta_{-,2}\zeta_{+,2}-\zeta_{-,3}\zeta_{+,3}-2)\tilde{t}^2+2(2(\tilde{u}-1)\zeta_{-,1}\zeta_{+,1}+(\tilde{u}-2)\zeta_{-,2}\zeta_{+,2}-\tilde{u}\zeta_{-,3}\zeta_{+,3}+2\zeta_{-,3}\zeta_{+,3}+2)\tilde{t}\\
&+\tilde{u}^2(\zeta_{-,2}\zeta_{+,2}-\zeta_{-,3}\zeta_{+,3}-2)-4\tilde{u}(\zeta_{-,1}\zeta_{+,1}+\zeta_{-,2}\zeta_{+,2}-\zeta_{-,3}\zeta_{+,3}-1)+4(3\zeta_{-,1}\zeta_{+,1}+3\zeta_{-,2}\zeta_{+,2}+\zeta_{-,3}\zeta_{+,3}+1))\tilde{s}\\
&+2(8\zeta_{-,3}\zeta_{+,3}\tilde{t}^2+8\tilde{t}^2-16\tilde{u}\zeta_{-,1}\zeta_{+,1}\tilde{t}+16\zeta_{-,1}\zeta_{+,1}\tilde{t}-16\tilde{u}\zeta_{-,2}\zeta_{+,2}\tilde{t}+16\zeta_{-,2}\zeta_{+,2}\tilde{t}\\
&+\sqrt{(\tilde{s}-4)\tilde{s}}\sqrt{-(\tilde{s}-4)(4m^2(\tilde{s}-4)-\tilde{s}^2+4\tilde{s}+(\tilde{t}-\tilde{u})^2)}\zeta_{-,3}\zeta_{+,2}\tilde{t}-(\tilde{s}-4)\sqrt{-\tilde{s}(4m^2(\tilde{s}-4)-\tilde{s}^2+4\tilde{s}+(\tilde{t}-\tilde{u})^2)}\zeta_{-,2}\zeta_{+,3}\tilde{t}\\
&-16\zeta_{-,3}\zeta_{+,3}\tilde{t}-16\tilde{t}+8\tilde{u}^2-16\tilde{u}+16\tilde{u}\zeta_{-,1}\zeta_{+,1}-16\zeta_{-,1}\zeta_{+,1}+16\tilde{u}\zeta_{-,2}\zeta_{+,2}\\
&-16\zeta_{-,2}\zeta_{+,2}-\sqrt{-\tilde{s}(4m^2(\tilde{s}-4)-\tilde{s}^2+4\tilde{s}+(\tilde{t}-\tilde{u})^2)}(\tilde{s}-4)\tilde{u}\zeta_{-,3}\zeta_{+,2}\\
&+\sqrt{(\tilde{s}-4)\tilde{s}}\sqrt{-(\tilde{s}-4)(4m^2(\tilde{s}-4)-\tilde{s}^2+4\tilde{s}+(\tilde{t}-\tilde{u})^2)}\tilde{u}\zeta_{-,2}\zeta_{+,3}+8\tilde{u}^2\zeta_{-,3}\zeta_{+,3}-16\tilde{u}\zeta_{-,3}\zeta_{+,3}+16\zeta_{-,3}\zeta_{+,3}+16))),
\end{aligned}
\tag{C6e}
$$

$$
\begin{aligned}
H_{23}=&\frac{16m}{(\tilde{s}-4)^2(\tilde{s}-4m^2)\sqrt{-(4m^2(\tilde{s}-4)-\tilde{s}^2+4\tilde{s}+(\tilde{t}-\tilde{u})^2)}}\sqrt{\tilde{s}}\\
&\times(-\tilde{s}^2(2\sqrt{(\tilde{s}-4)\tilde{s}}\sqrt{-(\tilde{s}-4)(4m^2(\tilde{s}-4)-\tilde{s}^2+4\tilde{s}+(\tilde{t}-\tilde{u})^2)}\\
&\times(\zeta_{-,2}\zeta_{+,3}-\zeta_{+,2}\zeta_{-,3})+\tilde{t}^3(\zeta_{-,1}\zeta_{+,1}-\zeta_{-,2}\zeta_{+,2}-\zeta_{-,3}\zeta_{+,3}+1)-3\tilde{t}^2\tilde{u}(\zeta_{-,1}\zeta_{+,1}-\zeta_{-,2}\zeta_{+,2}-\zeta_{-,3}\zeta_{+,3}+1)\\
&+3\tilde{t}\tilde{u}^2(\zeta_{-,1}\zeta_{+,1}-\zeta_{-,2}\zeta_{+,2}-\zeta_{-,3}\zeta_{+,3}+1)-16\tilde{t}(3\zeta_{-,1}\zeta_{+,1}+\zeta_{-,2}\zeta_{+,2}+\zeta_{-,3}\zeta_{+,3}+3)\\
&+\tilde{u}^3(-\zeta_{-,1}\zeta_{+,1}+\zeta_{-,2}\zeta_{+,2}+\zeta_{-,3}\zeta_{+,3}-1)+16\tilde{u}(3\zeta_{-,1}\zeta_{+,1}+\zeta_{-,2}\zeta_{+,2}+\zeta_{-,3}\zeta_{+,3}+3))\\
&+8\tilde{s}(\sqrt{(\tilde{s}-4)\tilde{s}}\sqrt{-(\tilde{s}-4)(4m^2(\tilde{s}-4)-\tilde{s}^2+4\tilde{s}+(\tilde{t}-\tilde{u})^2)}(\zeta_{-,2}\zeta_{+,3}-\zeta_{+,2}\zeta_{-,3})-8\tilde{t}(\zeta_{-,1}\zeta_{+,1}+\zeta_{-,2}\zeta_{+,2}\\
&+\zeta_{-,3}\zeta_{+,3}+1)+8\tilde{u}(\zeta_{-,1}\zeta_{+,1}+\zeta_{-,2}\zeta_{+,2}+\zeta_{-,3}\zeta_{+,3}+1)+\tilde{t}^3(\zeta_{-,1}\zeta_{+,1}+1)-3\tilde{t}^2(\zeta_{-,1}\zeta_{+,1}\tilde{u}+\tilde{u})\\
&+3\tilde{t}\tilde{u}^2(\zeta_{-,1}\zeta_{+,1}+1)-\tilde{u}^3(\zeta_{-,1}\zeta_{+,1}+1))-4(\tilde{t}-\tilde{u})^2(\sqrt{(\tilde{s}-4)\tilde{s}}\sqrt{-(\tilde{s}-4)(4m^2(\tilde{s}-4)-\tilde{s}^2+4\tilde{s}+(\tilde{t}-\tilde{u})^2)}\\
&\times(\zeta_{+,2}\zeta_{-,3}-\zeta_{-,2}\zeta_{+,3})+4\tilde{t}(\zeta_{-,1}\zeta_{+,1}+\zeta_{-,2}\zeta_{+,2}+\zeta_{-,3}\zeta_{+,3}+1)-4\tilde{u}(\zeta_{-,1}\zeta_{+,1}+\zeta_{-,2}\zeta_{+,2}+\zeta_{-,3}\zeta_{+,3}+1))\\
&-4m^2(\tilde{s}-4)(2(\tilde{s}-4)\sqrt{-\tilde{s}(4m^2(\tilde{s}-4)-\tilde{s}^2+4\tilde{s}+(\tilde{t}-\tilde{u})^2)}(\zeta_{+,2}\zeta_{-,3}-\zeta_{-,2}\zeta_{+,3})\\
&+(\tilde{s}-4)\tilde{t}(\tilde{s}(\zeta_{-,1}\zeta_{+,1}-\zeta_{-,2}\zeta_{+,2}-\zeta_{-,3}\zeta_{+,3}+1)-4(\zeta_{-,1}\zeta_{+,1}+\zeta_{-,2}\zeta_{+,2}+\zeta_{-,3}\zeta_{+,3}+1))\\
&-(\tilde{s}-4)\tilde{u}(\tilde{s}(\zeta_{-,1}\zeta_{+,1}-\zeta_{-,2}\zeta_{+,2}-\zeta_{-,3}\zeta_{+,3}+1)-4(\zeta_{-,1}\zeta_{+,1}+\zeta_{-,2}\zeta_{+,2}+\zeta_{-,3}\zeta_{+,3}+1)))\\
&+\tilde{s}^4(\tilde{t}-\tilde{u})(\zeta_{-,1}\zeta_{+,1}-\zeta_{-,2}\zeta_{+,2}-\zeta_{-,3}\zeta_{+,3}+1)-4\tilde{s}^3(\tilde{t}-\tilde{u})(3\zeta_{-,1}\zeta_{+,1}-\zeta_{-,2}\zeta_{+,2}-\zeta_{-,3}\zeta_{+,3}+3)),
\end{aligned}
\tag{C6f}
$$

$$
\begin{aligned}
H_{31}=&(8\tilde{s}(\tilde{s}^2\sqrt{-(\tilde{s}-4)(m^4-2m^2(\tilde{t}+1)+(\tilde{s}-2)\tilde{t}+\tilde{t}^2+1)}(\zeta_{-,1}\zeta_{+,3}+\zeta_{+,1}\zeta_{-,3})\\
&-2\tilde{s}(-\zeta_{-,1}\tilde{t}(\sqrt{-(m^4-2m^2(\tilde{t}+1)+(\tilde{s}-2)\tilde{t}+\tilde{t}^2+1)}\zeta_{+,3}\sqrt{(\tilde{s}-4)}+2\sqrt{(\tilde{s}-4)\tilde{s}}\zeta_{+,2})\\
&+(m^2+1)\zeta_{-,1}\zeta_{+,3}\sqrt{-(m^4-2m^2(\tilde{t}+1)+(\tilde{s}-2)\tilde{t}+\tilde{t}^2+1)}\sqrt{(\tilde{s}-4)}+\zeta_{+,1}\zeta_{-,3}(m^2-\tilde{t}+1)\\
&\times\sqrt{-(\tilde{s}-4)(m^4-2m^2(\tilde{t}+1)+(\tilde{s}-2)\tilde{t}+\tilde{t}^2+1)})+4\sqrt{(\tilde{s}-4)\tilde{s}}\zeta_{-,1}\zeta_{+,2}(m^4-2m^2(\tilde{t}+1)+(\tilde{t}-1)^2)\\
&-4\sqrt{(\tilde{s}-4)\tilde{s}}\zeta_{+,1}\zeta_{-,2}(m^4-2m^2(\tilde{t}+1)+(\tilde{s}-2)\tilde{t}+\tilde{t}^2+1)))\\
&/((\tilde{s}-4)\sqrt{(4m^2-\tilde{s})}\sqrt{m^4-2m^2(\tilde{t}+1)+(\tilde{s}-2)\tilde{t}+\tilde{t}^2+1}),
\end{aligned}
\tag{C6g}
$$

$$
\begin{aligned}
H_{32} = {} & \frac{16m}{(\tilde{s}-4)^2(\tilde{s}-4m^2)\sqrt{-(4m^2(\tilde{s}-4)-\tilde{s}^2+4\tilde{s}+(\tilde{t}-\tilde{u})^2)}} \\
& \times \sqrt{\tilde{s}}(\tilde{s}^2(2\sqrt{(\tilde{s}-4)\tilde{s}}\sqrt{-(\tilde{s}-4)(4m^2(\tilde{s}-4)-\tilde{s}^2+4\tilde{s}+(\tilde{t}-\tilde{u})^2)}(\zeta_{-,2}\zeta_{+,3}-\zeta_{+,2}\zeta_{-,3}) \\
& + \tilde{t}^3(\zeta_{-,1}\zeta_{+,1}-\zeta_{-,2}\zeta_{+,2}-\zeta_{-,3}\zeta_{+,3}+1) - 3\tilde{t}^2\tilde{u}(\zeta_{-,1}\zeta_{+,1}-\zeta_{-,2}\zeta_{+,2}-\zeta_{-,3}\zeta_{+,3}+1) + 3\tilde{t}\tilde{u}^2(\zeta_{-,1}\zeta_{+,1}-\zeta_{-,2}\zeta_{+,2} \\
& - \zeta_{-,3}\zeta_{+,3}+1) - 16\tilde{t}(3\zeta_{-,1}\zeta_{+,1}+\zeta_{-,2}\zeta_{+,2}+\zeta_{-,3}\zeta_{+,3}+3) + \tilde{u}^3(-\zeta_{-,1}\zeta_{+,1}+\zeta_{-,2}\zeta_{+,2}+\zeta_{-,3}\zeta_{+,3}-1) \\
& + 16\tilde{u}(3\zeta_{-,1}\zeta_{+,1}+\zeta_{-,2}\zeta_{+,2}+\zeta_{-,3}\zeta_{+,3}+3)) - 8\tilde{s}((\tilde{s}-4)\sqrt{-\tilde{s}(4m^2(\tilde{s}-4)-\tilde{s}^2+4\tilde{s}+(\tilde{t}-\tilde{u})^2)}(\zeta_{-,2}\zeta_{+,3}-\zeta_{+,2}\zeta_{-,3}) \\
& - 8\tilde{t}(\zeta_{-,1}\zeta_{+,1}+\zeta_{-,2}\zeta_{+,2}+\zeta_{-,3}\zeta_{+,3}+1) + 8\tilde{u}(\zeta_{-,1}\zeta_{+,1}+\zeta_{-,2}\zeta_{+,2}+\zeta_{-,3}\zeta_{+,3}+1) + \tilde{t}^3(\zeta_{-,1}\zeta_{+,1}+1) \\
& - 3\tilde{t}^2(\zeta_{-,1}\zeta_{+,1}\tilde{u}+\tilde{u}) + 3\tilde{t}\tilde{u}^2(\zeta_{-,1}\zeta_{+,1}+1) - \tilde{u}^3(\zeta_{-,1}\zeta_{+,1}+1)) \\
& + 4(\tilde{t}-\tilde{u})^2((\tilde{s}-4)\sqrt{-\tilde{s}(4m^2(\tilde{s}-4)-\tilde{s}^2+4\tilde{s}+(\tilde{t}-\tilde{u})^2)}(\zeta_{+,2}\zeta_{-,3}-\zeta_{-,2}\zeta_{+,3}) \\
& + 4\tilde{t}(\zeta_{-,1}\zeta_{+,1}+\zeta_{-,2}\zeta_{+,2}+\zeta_{-,3}\zeta_{+,3}+1) - 4\tilde{u}(\zeta_{-,1}\zeta_{+,1}+\zeta_{-,2}\zeta_{+,2}+\zeta_{-,3}\zeta_{+,3}+1)) \\
& + 4m^2(\tilde{s}-4)(2(\tilde{s}-4)\sqrt{-\tilde{s}(4m^2(\tilde{s}-4)-\tilde{s}^2+4\tilde{s}+(\tilde{t}-\tilde{u})^2)}(\zeta_{+,2}\zeta_{-,3}-\zeta_{-,2}\zeta_{+,3}) \\
& + (\tilde{s}-4)\tilde{t}(\tilde{s}(\zeta_{-,1}\zeta_{+,1}-\zeta_{-,2}\zeta_{+,2}-\zeta_{-,3}\zeta_{+,3}+1) - 4(\zeta_{-,1}\zeta_{+,1}+\zeta_{-,2}\zeta_{+,2}+\zeta_{-,3}\zeta_{+,3}+1)) \\
& - (\tilde{s}-4)\tilde{u}(\tilde{s}(\zeta_{-,1}\zeta_{+,1}-\zeta_{-,2}\zeta_{+,2}-\zeta_{-,3}\zeta_{+,3}+1) - 4(\zeta_{-,1}\zeta_{+,1}+\zeta_{-,2}\zeta_{+,2}+\zeta_{-,3}\zeta_{+,3}+1))) \\
& + \tilde{s}^4(-\tilde{t}+\tilde{u})(\zeta_{-,1}\zeta_{+,1}-\zeta_{-,2}\zeta_{+,2}-\zeta_{-,3}\zeta_{+,3}+1) + 4\tilde{s}^3(\tilde{t}-\tilde{u})(3\zeta_{-,1}\zeta_{+,1}-\zeta_{-,2}\zeta_{+,2}-\zeta_{-,3}\zeta_{+,3}+3)),
\end{aligned}
\tag{C6h}
$$

$$
\begin{aligned}
H_{33} = {} & \frac{1}{(\tilde{s}-4)^2(-4m^2+\tilde{s})} 8(8(\tilde{s}-4)^2(\zeta_{-,1}\zeta_{+,1}+\zeta_{-,2}\zeta_{+,2}-\zeta_{-,3}\zeta_{+,3}-1)m^6 \\
& - 2(\tilde{s}-4)^2(\tilde{s}(5\zeta_{-,1}\zeta_{+,1}-3\zeta_{-,2}\zeta_{+,2}-5\zeta_{-,3}\zeta_{+,3}+3)+4(\tilde{t}+\tilde{u}-2)(\zeta_{-,1}\zeta_{+,1}+\zeta_{-,2}\zeta_{+,2}-\zeta_{-,3}\zeta_{+,3}-1))m^4 \\
& + 2((\zeta_{-,1}\zeta_{+,1}-\zeta_{-,2}\zeta_{+,2}-\zeta_{-,3}\zeta_{+,3}+1)\tilde{s}^4 + (-6\zeta_{-,1}\zeta_{+,1}+10\zeta_{-,2}\zeta_{+,2}+14\zeta_{-,3}\zeta_{+,3} \\
& + \tilde{t}(\zeta_{-,1}\zeta_{+,1}+\zeta_{-,2}\zeta_{+,2}-\zeta_{-,3}\zeta_{+,3}-1)+\tilde{u}(\zeta_{-,1}\zeta_{+,1}+\zeta_{-,2}\zeta_{+,2}-\zeta_{-,3}\zeta_{+,3}-1)-2)\tilde{s}^3 + 2((\zeta_{-,2}\zeta_{+,2}-1)\tilde{t}^2 \\
& + 2((\tilde{u}-3)\zeta_{-,1}\zeta_{+,1}-3\zeta_{-,2}\zeta_{+,2}-\tilde{u}\zeta_{-,3}\zeta_{+,3}+3\zeta_{-,3}\zeta_{+,3}+3)\tilde{t}+\tilde{u}^2(\zeta_{-,2}\zeta_{+,2}-1) \\
& + 2(\zeta_{-,1}\zeta_{+,1}-7\zeta_{-,2}\zeta_{+,2}-17\zeta_{-,3}\zeta_{+,3}-9) - 6\tilde{u}(\zeta_{-,1}\zeta_{+,1}+\zeta_{-,2}\zeta_{+,2}-\zeta_{-,3}\zeta_{+,3}-1))\tilde{s}^2 - 8((\zeta_{-,2}\zeta_{+,2}-\zeta_{-,3}\zeta_{+,3}-2)\tilde{t}^2 \\
& + 2((2\tilde{u}-3)\zeta_{-,1}\zeta_{+,1}+(\tilde{u}-3)\zeta_{-,2}\zeta_{+,2}-\tilde{u}\zeta_{-,3}\zeta_{+,3}+3\zeta_{-,3}\zeta_{+,3}+3)\tilde{t}+\tilde{u}^2(\zeta_{-,2}\zeta_{+,2}-\zeta_{-,3}\zeta_{+,3}-2) \\
& - 6\tilde{u}(\zeta_{-,1}\zeta_{+,1}+\zeta_{-,2}\zeta_{+,2}-\zeta_{-,3}\zeta_{+,3}-1) - 16(\zeta_{-,3}\zeta_{+,3}+1))\tilde{s} - 4(8\zeta_{-,3}\zeta_{+,3}\tilde{t}^2+8\tilde{t}^2-16\tilde{u}\zeta_{-,1}\zeta_{+,1}\tilde{t}+16\zeta_{-,1}\zeta_{+,1}\tilde{t} \\
& - 16\tilde{u}\zeta_{-,2}\zeta_{+,2}\tilde{t}+16\zeta_{-,2}\zeta_{+,2}\tilde{t}+(\tilde{s}-4)\sqrt{-\tilde{s}(4m^2(\tilde{s}-4)-\tilde{s}^2+4\tilde{s}+(\tilde{t}-\tilde{u})^2)}\zeta_{-,3}\zeta_{+,2}\tilde{t} \\
& - \sqrt{-\tilde{s}(4m^2(\tilde{s}-4)-\tilde{s}^2+4\tilde{s}+(\tilde{t}-\tilde{u})^2)}(\tilde{s}-4)\zeta_{-,2}\zeta_{+,3}\tilde{t} - 16\zeta_{-,3}\zeta_{+,3}\tilde{t} - 16\tilde{t}+8\tilde{u}^2-16\tilde{u}+16\tilde{u}\zeta_{-,1}\zeta_{+,1} \\
& - 16\zeta_{-,1}\zeta_{+,1}+16\tilde{u}\zeta_{-,2}\zeta_{+,2} - 16\zeta_{-,2}\zeta_{+,2} - (\tilde{s}-4)\sqrt{-\tilde{s}(4m^2(\tilde{s}-4)-\tilde{s}^2+4\tilde{s}+(\tilde{t}-\tilde{u})^2)}\tilde{u}\zeta_{-,3}\zeta_{+,2} \\
& + \sqrt{(\tilde{s}-4)\tilde{s}}\sqrt{-(\tilde{s}-4)(4m^2(\tilde{s}-4)-\tilde{s}^2+4\tilde{s}+(\tilde{t}-\tilde{u})^2)}\tilde{u}\zeta_{-,2}\zeta_{+,3} + 8\tilde{u}^2\zeta_{-,3}\zeta_{+,3} - 16\tilde{u}\zeta_{-,3}\zeta_{+,3} \\
& + 16\zeta_{-,3}\zeta_{+,3}+16))m^2 - \tilde{s}(2(\zeta_{-,1}\zeta_{+,1}+\zeta_{-,2}\zeta_{+,2}+\zeta_{-,3}\zeta_{+,3}+1)\tilde{s}^3 + ((\zeta_{-,1}\zeta_{+,1}-\zeta_{-,3}\zeta_{+,3})\tilde{t}^2 - 2(-\zeta_{-,2}\zeta_{+,2}\tilde{u}+\tilde{u} \\
& + \zeta_{-,1}\zeta_{+,1}+\zeta_{-,2}\zeta_{+,2}-\zeta_{-,3}\zeta_{+,3}-1)\tilde{t}+\tilde{u}^2(\zeta_{-,1}\zeta_{+,1}-\zeta_{-,3}\zeta_{+,3}) - 2\tilde{u}(\zeta_{-,1}\zeta_{+,1}+\zeta_{-,2}\zeta_{+,2}-\zeta_{-,3}\zeta_{+,3}-1)
\end{aligned}
$$

$$-2(7\zeta_{-,1}\zeta_{+,1}+7\zeta_{-,2}\zeta_{+,2}+9\zeta_{-,3}\zeta_{+,3}+9))\tilde{s}^2-4((2\zeta_{-,1}\zeta_{+,1}+\zeta_{-,2}\zeta_{+,2}-\zeta_{-,3}\zeta_{+,3})\tilde{t}^2+2(-2\zeta_{-,1}\zeta_{+,1}-2\zeta_{-,2}\zeta_{+,2}+2\zeta_{-,3}\zeta_{+,3}$$
$$+\tilde{u}(\zeta_{-,2}\zeta_{+,2}-\zeta_{-,3}\zeta_{+,3}-2)+2)\tilde{t}-4\tilde{u}(\zeta_{-,1}\zeta_{+,1}+\zeta_{-,2}\zeta_{+,2}-\zeta_{-,3}\zeta_{+,3}-1)+\tilde{u}^2(2\zeta_{-,1}\zeta_{+,1}+\zeta_{-,2}\zeta_{+,2}-\zeta_{-,3}\zeta_{+,3})$$
$$-4(\zeta_{-,1}\zeta_{+,1}+\zeta_{-,2}\zeta_{+,2}+3\zeta_{-,3}\zeta_{+,3}+3))\tilde{s}+2(8\zeta_{-,1}\zeta_{+,1}\tilde{t}^2+8\zeta_{-,2}\zeta_{+,2}\tilde{t}^2-16\tilde{t}\tilde{u}-16\zeta_{-,1}\zeta_{+,1}\tilde{t}-16\zeta_{-,2}\zeta_{+,2}\tilde{t}$$
$$+\sqrt{-\tilde{s}(4m^2(\tilde{s}-4)-\tilde{s}^2+4\tilde{s}+(\tilde{t}-\tilde{u})^2)}(\tilde{s}-4)\zeta_{-,3}\zeta_{+,2}\tilde{t}-\sqrt{(\tilde{s}-4)\tilde{s}}\sqrt{-(\tilde{s}-4)(4m^2(\tilde{s}-4)-\tilde{s}^2+4\tilde{s}+(\tilde{t}-\tilde{u})^2)}\zeta_{-,2}\zeta_{+,3}\tilde{t}$$
$$-16\tilde{u}\zeta_{-,3}\zeta_{+,3}\tilde{t}+16\zeta_{-,3}\zeta_{+,3}\tilde{t}+16\tilde{t}+16\tilde{u}+8\tilde{u}^2\zeta_{-,1}\zeta_{+,1}-16\tilde{u}\zeta_{-,1}\zeta_{+,1}+16\zeta_{-,1}\zeta_{+,1}+8\tilde{u}^2\zeta_{-,2}\zeta_{+,2}-16\tilde{u}\zeta_{-,2}\zeta_{+,2}+16\zeta_{-,2}\zeta_{+,2}$$
$$-(\tilde{s}-4)\sqrt{-\tilde{s}(4m^2(\tilde{s}-4)-\tilde{s}^2+4\tilde{s}+(\tilde{t}-\tilde{u})^2)}\tilde{u}\zeta_{-,3}\zeta_{+,2}+(\tilde{s}-4)\sqrt{-\tilde{s}(4m^2(\tilde{s}-4)-\tilde{s}^2+4\tilde{s}+(\tilde{t}-\tilde{u})^2)}\tilde{u}\zeta_{-,2}\zeta_{+,3}$$
$$+16\tilde{u}\zeta_{-,3}\zeta_{+,3}-16\zeta_{-,3}\zeta_{+,3}-16))). \tag{C6i}$$

[1] T. P. Gorringe and D. W. Hertzog, Precision muon physics, Prog. Part. Nucl. Phys. **84**, 73 (2015).

[2] W. H. Breunlich, P. Kammel, J. S. Cohen, and M. Leon, Muon-catalyzed fusion, Annu. Rev. Nucl. Part. Sci. **39**, 311 (1989).

[3] A. Yaouanc and P. D. de Réotier, *Muon Spin Rotation, Relaxation, and Resonance: Applications to Condensed Matter* (Oxford University Press, Oxford, 2011).

[4] S. J. Blundell, Spin-polarized muons in condensed matter physics, Contemp. Phys. **40**, 175 (1999).

[5] T. Aoyama, N. Asmussen, M. Benayoun, J. Bijnens, T. Blum, M. Bruno, I. Caprini, C. C. Calame, M. Ce, G. Colangelo *et al.*, The anomalous magnetic moment of the muon in the standard model, Phys. Rep. **887**, 1 (2020).

[6] Borsanyi, Sz, Z. Fodor, J. N. Guenther, C. Hoelbling, S. D. Katz, L. Lellouch, T. Lippert, K. Miura, L. Parato, K. K. Szabo *et al.*, Leading hadronic contribution to the muon magnetic moment from lattice QCD, Nature (London) **593**, 51 (2021).

[7] B. Abi, T. Albahri, S. Al-Kilani, D. Allspach, L. P. Alonzi, A. Anastasi, A. Anisenkov, F. Azfar, K. Badgley, S. Baeßler *et al.* (Muon $g-2$ Collaboration), Measurement of the Positive Muon Anomalous Magnetic Moment to 0.46 ppm, Phys. Rev. Lett. **126**, 141801 (2021).

[8] Y. Kuno and Y. Okada, Muon decay and physics beyond the standard model, Rev. Mod. Phys. **73**, 151 (2001).

[9] F. Renga, Experimental searches for muon decays beyond the standard model, Rev. Phys. **4**, 100029 (2019).

[10] M. M. Alsharoa, C. M. Ankenbrandt, M. Atac, B. R. Autin, V. I. Balbekov, V. D. Barger, O. Benary, J. R. J. Bennett, M. S. Berger, J. S. Berg *et al.*, Recent progress in neutrino factory and muon collider research within the muon collaboration, Phys. Rev. ST Accel. Beams **6**, 081001 (2003).

[11] A. Bandyopadhyay, S. Choubey, R. Gandhi, S. Goswami, B. L. Roberts, J. Bouchez, I. Antoniadis, J. Ellis, G. F. Giudice, T. Schwetz *et al.*, Physics at a future neutrino factory and super-beam facility, Rep. Prog. Phys. **72**, 106201 (2009).

[12] M. Boscolo, J. P. Delahaye, and M. Palmer, The future prospects of muon colliders and neutrino factories, Rev. Accel. Sci. Techol. **10**, 189 (2019).

[13] A. Blondel, Muon polarisation in the neutrino factory, Nucl. Instrum. Methods Phys. Res., Sect. A **451**, 131 (2000).

[14] S. Y. Choi, M. Drees, B. Gaissmaier, and J. S. Lee, CP violation in tau slepton pair production at muon colliders, Phys. Rev. D **64**, 095009 (2001).

[15] O. Kittel and F. von der Pahlen, *CP*-violating Higgs boson mixing in chargino production at the muon collider, J. High Energy Phys. 08 (2008) 030.

[16] A. Toyoda, K. Ishida, K. Shimomura, S. N. Nakamura, Y. Matsuda, W. Higemoto, T. Matsuzaki, and K. Nagamine, New Insights in Muon-Catalyzed *dd* Fusion by Using Ortho-Para Controlled Solid Deuterium, Phys. Rev. Lett. **90**, 243401 (2003).

[17] L. Holmlid, Existing source for muon-catalyzed nuclear fusion can give megawatt thermal fusion generator, Fusion Sci. Technol. **75**, 208 (2019).

[18] K. Pachucki and A. Wienczek, Nuclear structure effects in light muonic atoms, Phys. Rev. A **91**, 040503(R) (2015).

[19] C. Ji, S. Bacca, N. Barnea, O. J. Hernandez, and N. Nevo-Dinur, *Ab initio* calculation of nuclear-structure corrections in muonic atoms, J. Phys. G **45**, 093002 (2018).

[20] I. Hashim, H. Ejiri, F. Othman, F. Ibrahim, F. Soberi, N. Ghani, T. Shima, A. Sato, and K. Ninomiya, Nuclear isotope production by ordinary muon capture reaction, Nucl. Instrum. Methods Phys. Res., Sect. A **963**, 163749 (2020).

[21] D. Adams, B. Adeva, E. Arik, A. Arvidson, B. Badelek, M. K. Ballintijn, G. Bardin, G. Baum, P. Berglund, L. Betev *et al.*, Spin structure of the proton from polarized inclusive deep-inelastic muon-proton scattering, Phys. Rev. D **56**, 5330 (1997).

[22] M. Aghasyan, M. G. Alexeev, G. D. Alexeev, A. Amoroso, V. Andrieux, N. V. Anfimov, V. Anosov, A. Antoshkin, K. Augsten, W. Augustyniak *et al.*, Transverse-momentum-

dependent multiplicities of charged hadrons in muon-deuteron deep inelastic scattering, Phys. Rev. D **97**, 032006 (2018).
[23] V. Brudanin, V. Egorov, T. Filipova, A. Kachalkin, V. Kovalenko, A. Salamatin, Y. Shitov, I. Štekl, S. Vassiliev, V. Vorobel *et al.*, Measurement of the induced pseudoscalar form factor in the capture of polarized muons by Si nuclei, Nucl. Phys. **A587**, 577 (1995).
[24] D. F. Measday, The nuclear physics of muon capture, Phys. Rep. **354**, 243 (2001).
[25] D. Louca, G. J. MacDougall, and T. J. Williams, US Muon Workshop 2021: A road map for a future Muon Facility, arXiv:2110.09479.
[26] S. Cook, R. D'Arcy, A. Edmonds, M. Fukuda, K. Hatanaka, Y. Hino, Y. Kuno, M. Lancaster, Y. Mori, T. Ogitsu, H. Sakamoto, A. Sato, N. H. Tran, N. M. Truong, M. Wing, A. Yamamoto, and M. Yoshida, Delivering the world's most intense muon beam, Phys. Rev. Accel. Beams **20**, 030101 (2017).
[27] G. H. Eaton and S. H. Kilcoyne, Muon production: Past, present and future, in *Muon Science* (Routledge, New York, 2017), pp. 11–37.
[28] B. Norum and R. Rossmanith, Polarized beams in a muon collider, Nucl. Phys. B, Proc. Suppl. **51**, 191 (1996).
[29] P. Bakule and E. Morenzoni, Generation and applications of slow polarized muons, Contemp. Phys. **45**, 203 (2004).
[30] A. A. Sahai, T. Tajima, and V. D. Shiltsev, Schemes of laser muon acceleration: Ultra-short, micron-scale beams, Int. J. Mod. Phys. A **34**, 1943008 (2019).
[31] C. N. Danson, C. Haefner, J. Bromage, T. Butcher, J.-C. F. Chanteloup, E. A. Chowdhury, A. Galvanauskas, L. A. Gizzi, J. Hein, D. I. Hillier *et al.*, Petawatt and exawatt class lasers worldwide, High Power Laser Sci. Eng. **7**, e54 (2019).
[32] J. W. Yoon, C. Jeon, J. Shin, S. K. Lee, H. W. Lee, I. W. Choi, H. T. Kim, J. H. Sung, and C. H. Nam, Achieving the laser intensity of 5.5×10^{22} W/cm^2 with a wavefront-corrected multi-PW laser, Opt. Express **27**, 20412 (2019).
[33] J. W. Yoon, Y. G. Kim, I. W. Choi, J. H. Sung, H. W. Lee, S. K. Lee, and C. H. Nam, Realization of laser intensity over 10^{23} W/cm^2, Optica **8**, 630 (2021).
[34] A. Higginson, R. J. Gray, M. King, R. J. Dance, S. Williamson, N. Butler, R. Wilson, R. Capdessus, C. Armstrong, and J. S. Green, Near-100 MeV protons via a laser-driven transparency-enhanced hybrid acceleration scheme, Nat. Commun. **9**, 724 (2018).
[35] A. McIlvenny, D. Doria, L. Romagnani, H. Ahmed, N. Booth, E. J. Ditter, O. C. Ettlinger, G. S. Hicks, P. Martin, G. G. Scott, S. D. R. Williamson, A. Macchi, P. McKenna, Z. Najmudin, D. Neely, S. Kar, and M. Borghesi, Selective Ion Acceleration by Intense Radiation Pressure, Phys. Rev. Lett. **127**, 194801 (2021).
[36] A. J. Gonsalves *et al.*, Petawatt Laser Guiding and Electron Beam Acceleration to 8 GeV in a Laser-Heated Capillary Discharge Waveguide, Phys. Rev. Lett. **122**, 084801 (2019).
[37] Z. Gong, Y. Shou, Y. Tang, and X. Yan, Energetic spin-polarized proton beams from two-stage coherent acceleration in laser-driven plasma, Phys. Rev. E **102**, 053212 (2020).
[38] L. Jin, M. Wen, X. Zhang, A. Hützen, J. Thomas, M. Büscher, and B. Shen, Spin-polarized proton beam generation from gas-jet targets by intense laser pulses, Phys. Rev. E **102**, 011201(R) (2020).
[39] X. F. Li, P. Gibbon, A. Hützen, M. Büscher, S. M. Weng, M. Chen, and Z. M. Sheng, Polarized proton acceleration in ultraintense laser interaction with near-critical-density plasmas, Phys. Rev. E **104**, 015216 (2021).
[40] M. Wen, M. Tamburini, and C. H. Keitel, Polarized Laser-Wakefield-Accelerated Kiloampere Electron Beams, Phys. Rev. Lett. **122**, 214801 (2019).
[41] Y. Wu, L. Ji, X. Geng, Q. Yu, N. Wang, B. Feng, Z. Guo, W. Wang, C. Qin, X. Yan, L. Zhang, J. Thomas, A. Hützen, A. Pukhov, M. Büscher, B. Shen, and R. Li, Polarized electron acceleration in beam-driven plasma wakefield based on density down-ramp injection, Phys. Rev. E **100**, 043202 (2019).
[42] Z. Nie, F. Li, F. Morales, S. Patchkovskii, O. Smirnova, W. An, N. Nambu, D. Matteo, K. A. Marsh, F. Tsung, W. B. Mori, and C. Joshi, In Situ Generation of High-Energy Spin-Polarized Electrons in a Beam-Driven Plasma Wakefield Accelerator, Phys. Rev. Lett. **126**, 054801 (2021).
[43] Y.-F. Li, R. Shaisultanov, K. Z. Hatsagortsyan, F. Wan, C. H. Keitel, and J.-X. Li, Ultrarelativistic Electron-Beam Polarization in Single-Shot Interaction with an Ultraintense Laser Pulse, Phys. Rev. Lett. **122**, 154801 (2019).
[44] F. Wan, R. Shaisultanov, Y.-F. Li, K. Z. Hatsagortsyan, C. H. Keitel, and J.-X. Li, Ultrarelativistic polarized positron jets via collision of electron and ultraintense laser beams, Phys. Lett. B **800**, 135120 (2020).
[45] D. Seipt, D. Del Sorbo, C. P. Ridgers, and A. G. R. Thomas, Ultrafast polarization of an electron beam in an intense bichromatic laser field, Phys. Rev. A **100**, 061402(R) (2019).
[46] H.-H. Song, W.-M. Wang, J.-X. Li, Y.-F. Li, and Y.-T. Li, Spin-polarization effects of an ultrarelativistic electron beam in an ultraintense two-color laser pulse, Phys. Rev. A **100**, 033407 (2019).
[47] Y.-Y. Chen, P.-L. He, R. Shaisultanov, K. Z. Hatsagortsyan, and C. H. Keitel, Polarized Positron Beams via Intense Two-Color Laser Pulses, Phys. Rev. Lett. **123**, 174801 (2019).
[48] W.-Y. Liu, K. Xue, F. Wan, M. Chen, J.-X. Li, F. Liu, S.-M. Weng, Z.-M. Sheng, and J. Zhang, Trapping and acceleration of spin-polarized positrons from γ photon splitting in wakefields, Phys. Rev. Research **4**, L022028 (2022).
[49] Y.-F. Li, Y.-Y. Chen, W.-M. Wang, and H.-S. Hu, Production of Highly Polarized Positron Beams via Helicity Transfer from Polarized Electrons in a Strong Laser Field, Phys. Rev. Lett. **125**, 044802 (2020).
[50] K. Xue, R.-T. Guo, F. Wan, R. Shaisultanov, Y.-Y. Chen, Z.-F. Xu, X.-G. Ren, K. Z. Hatsagortsyan, C. H. Keitel, and J.-X. Li, Generation of arbitrarily polarized GeV lepton beams via nonlinear Breit-Wheeler process, Fundam. Res. (to be published).
[51] K. Ta Phuoc, S. Corde, C. Thaury, V. Malka, A. Tafzi, J. P. Goddet, R. C. Shah, S. Sebban, and A. Rousse, All-optical Compton gamma-ray source, Nat. Photonics **6**, 308 (2012).
[52] Y.-F. Li, R. Shaisultanov, Y.-Y. Chen, F. Wan, K. Z. Hatsagortsyan, C. H. Keitel, and J.-X. Li, Polarized Ultrashort Brilliant Multi-GeV γ Rays via Single-Shot Laser-Electron Interaction, Phys. Rev. Lett. **124**, 014801 (2020).

[53] D. Abbott, P. Adderley, A. Adeyemi, P. Aguilera, M. Ali, H. Areti, M. Baylac, J. Benesch, G. Bosson, B. Cade *et al.* (PEPPo Collaboration), Production of Highly Polarized Positrons Using Polarized Electrons at MeV Energies, Phys. Rev. Lett. **116**, 214801 (2016).

[54] W.-Q. Wei, F. Wan, Y. I. Salamin, J.-R. Ren, K. Z. Hatsagortsyan, C. H. Keitel, J.-X. Li, and Y.-T. Zhao, All-optical ultrafast spin rotation for relativistic charged particle beams, arXiv:2201.05128.

[55] H. Athar, G. L. Lin, and J. J. Tseng, Muon pair production by electron-photon scatterings, Phys. Rev. D **64**, 071302(R) (2001).

[56] L. Serafini, I. Drebot, A. Bacci, F. Broggi, C. Curatolo, A. Marocchino, N. Panzeri, V. Petrillo, A. R. Rossi, and M. R. Conti, A muon source based on plasma accelerators, Nucl. Instrum. Methods Phys. Res., Sect. A **909**, 309 (2018).

[57] M. Antonelli, M. Boscolo, R. Di Nardo, and P. Raimondi, Novel proposal for a low emittance muon beam using positron beam on target, Nucl. Instrum. Methods Phys. Res., Sect. A **807**, 101 (2016).

[58] M. Boscolo, M. Antonelli, O. R. Blanco-García, S. Guiducci, S. Liuzzo, P. Raimondi, and F. Collamati, Low emittance muon accelerator studies with production from positrons on target, Phys. Rev. Accel. Beams **21**, 061005 (2018).

[59] M. Boscolo, M. Antonelli, A. Ciarma, and P. Raimondi, Muon production and accumulation from positrons on target, Phys. Rev. Accel. Beams **23**, 051001 (2020).

[60] B. S. Rao, J. H. Jeon, H. T. Kim, and C. H. Nam, Bright muon source driven by GeV electron beams from a compact laser wakefield accelerator, Plasma Phys. Control. Fusion **60**, 095002 (2018).

[61] J. W. Motz, H. A. Olsen, and H. W. Koch, Pair production by photons, Rev. Mod. Phys. **41**, 581 (1969).

[62] K. I. Hikasa, Transverse-polarization effects in e^+e^- collisions: The role of chiral symmetry, Phys. Rev. D **33**, 3203 (1986).

[63] Q. Zhao, L. Tang, F. Wan, B.-C. Liu, R.-Y. Liu, R.-Z. Yang, J.-Q. Yu, X.-G. Ren, Z.-F. Xu, Y.-T. Zhao, Y.-S. Huang, and J.-X. Li, Signatures of linear Breit-Wheeler pair production in polarized $\gamma\gamma$ collisions, Phys. Rev. D **105**, L071902 (2022).

[64] V. B. Berestetskii, E. M. Lifshitz, and L. P. Pitaevskii, *Quantum Electrodynamics* (Pergamon, Oxford, 1982).

[65] W. Greiner and J. Reinhardt, *Quantum Electrodynamics* (Springer Science & Business Media, New York, 2008).

[66] G. W. Ford and C. J. Mullin, Scattering of polarized dirac particles on electrons, Phys. Rev. **108**, 477 (1957).

[67] A. Rączka and R. Rączka, Møller scattering of arbitrarily polarized electrons, Phys. Rev. **110**, 1469 (1958).

[68] G. L. Kotkin, S. I. Polityko, and V. G. Serbo, Polarization of final electrons in the Compton effect, Nucl. Instrum. Methods Phys. Res., Sect. A **405**, 30 (1998).

[69] F. Del Gaudio, T. Grismayer, R. A. Fonseca, and L. O. Silva, Compton scattering in particle-in-cell codes, J. Plasma Phys. **86**, 905860516 (2020).

[70] L. Esnault, E. d'Humières, A. Arefiev, and X. Ribeyre, Electron-positron pair production in the collision of real photon beams with wide energy distributions, Plasma Phys. Control. Fusion **63**, 125015 (2021).

[71] W. Herr and B. Muratori, Concept of luminosity, in *Proceedings of CAS-CERN Accelerator School: Intermediate Course on Accelerator Physics*, edited by D. Brandt (CERN, Geneva, Switzerland, 2006), pp. 361–377.

[72] J. Esberg, U. I. Uggerhøj, B. Dalena, and D. Schulte, Strong field processes in beam-beam interactions at the Compact Linear Collider, Phys. Rev. ST Accel. Beams **17**, 051003 (2014).

[73] C. B. Schroeder, E. Esarey, C. G. R. Geddes, C. Benedetti, and W. P. Leemans, Physics considerations for laser-plasma linear colliders, Phys. Rev. ST Accel. Beams **13**, 101301 (2010).

[74] C. B. Schroeder, E. Esarey, and W. P. Leemans, Beamstrahlung considerations in laser-plasma-accelerator-based linear colliders, Phys. Rev. ST Accel. Beams **15**, 051301 (2012).

[75] K. Nakajima, J. Wheeler, G. Mourou, and T. Tajima, Novel laser-plasma TeV electron-positron linear colliders, Int. J. Mod. Phys. A **34**, 1943003 (2019).

[76] V. Shiltsev and F. Zimmermann, Modern and future colliders, Rev. Mod. Phys. **93**, 015006 (2021).

[77] X. L. Wang, Z. Y. Xu, W. Luo, H. Y. Lu, Z. C. Zhu, and X. Q. Yan, Transmutation prospect of long-lived nuclear waste induced by high-charge electron beam from laser plasma accelerator, Phys. Plasmas **24**, 093105 (2017).

[78] Y. Ma, J. Zhao, Y. Li, D. Li, L. Chen, J. Liu, S. J. D. Dann, Y. Ma, X. Yang, Z. Ge, Z. Sheng, and J. Zhang, Ultrahigh-charge electron beams from laser-irradiated solid surface, Proc. Natl. Acad. Sci. U.S.A. **115**, 6980 (2018).

[79] J. Götzfried, A. Döpp, M. F. Gilljohann, F. M. Foerster, H. Ding, S. Schindler, G. Schilling, A. Buck, L. Veisz, and S. Karsch, Physics of High-Charge Electron Beams in Laser-Plasma Wakefields, Phys. Rev. X **10**, 041015 (2020).

[80] J. L. Shaw, M. A. Romo-Gonzalez, N. Lemos, P. M. King, G. Bruhaug, K. G. Miller, C. Dorrer, B. Kruschwitz, L. Waxer, G. J. Williams *et al.*, Microcoulomb ($0.7 \pm \frac{0.4}{0.2}$ μC) laser plasma accelerator on OMEGA EP, Sci. Rep. **11**, 7498 (2021).

[81] A. Alejo, R. Walczak, and G. Sarri, Laser-driven high-quality positron sources as possible injectors for plasma-based accelerators, Sci. Rep. **9**, 5279 (2019).

[82] A. Alejo, G. M. Samarin, J. R. Warwick, and G. Sarri, Laser-wakefield electron beams as drivers of high-quality positron beams and inverse-Compton-scattered photon beams, Front. Phys. **7**, 49 (2019).

[83] A. A. Sahai, Quasimonoenergetic laser plasma positron accelerator using particle-shower plasma-wave interactions, Phys. Rev. Accel. Beams **21**, 081301 (2018).

[84] S. Diederichs, C. Benedetti, E. Esarey, J. Osterhoff, and C. B. Schroeder, High-quality positron acceleration in beam-driven plasma accelerators, Phys. Rev. Accel. Beams **23**, 121301 (2020).

[85] S. Zhou, J. Hua, W. An, W. B. Mori, C. Joshi, J. Gao, and W. Lu, High Efficiency Uniform Wakefield Acceleration of a Positron Beam Using Stable Asymmetric Mode in a Hollow Channel Plasma, Phys. Rev. Lett. **127**, 174801 (2021).